Planetary and Space Science 101 (2014) 37–52

Contents lists available at ScienceDirect

Planetary and Space Science

journal homepage: www.elsevier.com/locate/pss

# Geological features and evolution history of Sinus Iridum, the Moon

Le Qiao [a], Long Xiao [a,*], Jiannan Zhao [a], Qian Huang [a], Junichi Haruyama [b]

[a] Planetary Science Institute, China University of Geosciences, Wuhan 430074, China
[b] ISAS, JAXA, 3-1-1 Yoshino-dai, Chuo-ku, Sagamihara, Kanagawa 252-5210, Japan

ARTICLE INFO

*Article history:*
Received 9 June 2013
Received in revised form
2 March 2014
Accepted 11 June 2014
Available online 25 June 2014

*Keywords:*
Sinus Iridum
Moon
Geological features
Magmatic activities
Lunar exploration

ABSTRACT

The Sinus Iridum region is one of the important candidate landing areas for the future Chinese lunar robotic and human missions. Considering its flat topography, abundant geomorphic features and complex evolutionary history, this region shows great significance to both lunar science and landing exploration, including powered descent, surface trafficability and in-situ exploration. First, we use Lunar Reconnaissance Orbiter (LRO) Altimeter (LOLA) and Camera (LROC) data to characterize regional topographic and geomorphological features within Sinus Iridum, e.g., wrinkle ridges and sinuous rilles. Then, we deduce the iron and titanium content for the mare surface using the Clementine ultraviolet–visible (UVVIS) data and generate mineral absorption features using the Chandrayaan-1 Moon Mineralogy Mapper ($M^3$) spectrometer data. Later, we date the mare surface using crater size-frequency distribution (CSFD) method. CSFD measurements show that this region has experienced four major lava infilling events with model ages ranging from 3.32 Ga to 2.50 Ga. The regional magmatic activities evolved from Imbrian-aged low-titanium to Eratosthenian-aged medium-titanium. The inner Sinus Iridum is mainly composed of pyroxene-rich basalts with olivine abundance increasing with time, while the surrounding highlands have a feldspar-dominated composition. In the northern wall of Sinus Iridum, some potential olivine-rich materials directly excavated from the lunar mantle are visible. The Sinus Iridum region is an ideal target for future landing exploration, we propose two candidate landing sites for the future Chinese robotic and human missions.

© 2014 Elsevier Ltd. All rights reserved.

## 1. Introduction

Sinus Iridum is a flat mare region located to the northwest Mare Imbrium on the nearside of the Moon. Considering its flat topography, Sinus Iridum has been selected as one of the important candidate landing areas for the future Chinese robotic and human exploration missions, e.g., Chang'E-5 lunar sample return mission (Qiu and Stone, 2013). Previous studies suggested this region had experienced complex evolutionary history because of the abundant geomorphic features on the surface, including wrinkle ridges, sinuous rilles, impact craters and crater chains, making this region attractive for lunar geology research (e.g., Chen et al., 2010; Gong and Jin, 2012; Huang et al., 2010; Schaber, 1969; Zou, 2011).

The Montes Jura (Fig. 1) surrounding the Sinus Iridum was likely formed by accumulating of ejecta from the Sinus Iridum impact (e.g., Schaber, 1969). The numerous small craters scattered in the inner Sinus Iridum were mainly results of impact activities after the magmatic activities ceased, including both primary and secondary impacts. While the wrinkle ridges present in the connecting region of Sinus Iridum and Mare Imbrium are generally considered to be tectonic landforms which originated from basin-localized folding and faulting over thrust faults (e.g., Maxwell, 1978; Golombek et al., 1991; Watters, 2004). The sinuous rilles distributed in the mare region are thought to be formed by magmatic activities, but the exact formation model is still debated (e.g., Carr, 1974; Hulme, 1973; Hurwitz et al., 2012; Williams et al., 2000). The low spatial resolution of earlier topographic and imagery data prevented the high-resolution quantitative descriptions (sub-meter scale) of these sinuous rilles, which are essential for exploration of their formation. Wilson and Head (1981) developed mathematical models for thermal erosion origin for sinuous rilles and placed constraints on the eruption rates needed to form the rilles. Siewert and Ferlito (2008) investigated the 2001 eruption on Mount Etna, and developed a model for the mechanical erosion origin for the observed sinuous rilles. While Spudis et al. (1988) combined the studies of terrestrial lava tube systems and detailed site geology of the Apollo 15 areas, and proposed that the Hadley Rille was primary constructional features that developed along preexisting structural depressions without substantial thermal or mechanical erosion.

Schaber (1969) concluded that the Sinus Iridum was formed by a large impact after the Imbrium impact which formed the Imbrium basin. Massive ejecta accumulated around the Iridum crater, forming the present Montes Jura. Crater rim and pre-cratering materials slumped into the crater shaping the crater

* Corresponding author. Tel.: +86 27 6788 3398.
*E-mail addresses:* le.qiao@cug.edu.cn (L. Qiao), longxiao@cug.edu.cn (L. Xiao), jnzhao@cug.edu.cn (J. Zhao), qianhuang@cug.edu.cn (Q. Huang), haruyama.junichi@jaxa.jp (J. Haruyama).

http://dx.doi.org/10.1016/j.pss.2014.06.007
0032-0633/© 2014 Elsevier Ltd. All rights reserved.

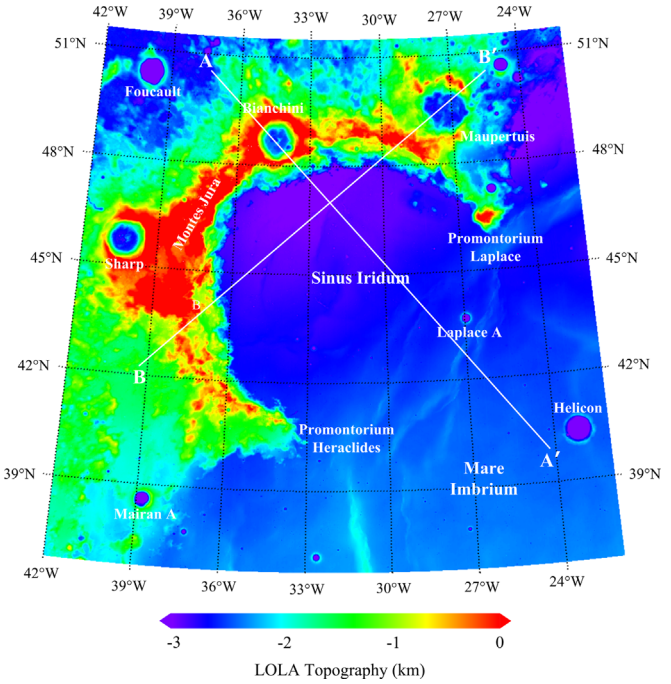



**Fig. 1.** LOLA topographic data for the Sinus Iridum and surrounding areas. Some key geographic features are labeled with their names, e.g., Montes Jura and Promontorium Laplace. The white solid lines show the location of elevation profiles derived from LOLA topography (Fig. 2). The map projection is Lambert conformal projection, the standard parallels are 42°N and 47°N, and the central meridian is 32°W, up is the north.

wall as steep as we observe now. Filling of basalts in the Sinus Iridum and northwestern Imbrium basin was another major event after the deposition of Iridum impact ejecta. Large amount of basalt flows covered not only the initial crater floor, but also the southeastern part of the primitive Montes Jura and the inner ring of the Imbrium basin. The thickness of mare basalts in the Sinus Iridum was estimated to be about 500 m using the relationship between craters' diameter and depth (Thomson et al., 2009).

This region has experienced several episodes of magmatic activity, indicating a complex and multi-stage evolutionary history. However, due to the limited resolution of imagery data predating Lunar Reconnaissance Orbiter Camera (LROC) images, previous research showed some inconsistency about the geographic extent and time range of these multiple magma filling events. Hiesinger et al. (2000) separated the mare basalts of Sinus Iridum region into four spectral homogeneous units based on the Galileo Earth/Moon Encounter 2 (EM2) multispectral imagery data, and determined the surface age for these units as 3.39–2.96 Ga. Although the Hiesinger et al. (2000) dating results were consistent with the stratigraphic classification described in Schaber (1969), these two studies showed inconsistency of the geographic extent of these multiple magmatic activities. Based on Clementine UVVIS multispectral imaging data, iron and titanium content maps, Bugiolacchi and Guest (2008) divided the inner Sinus Iridum into three units, and calculated surface age of the three units as 3.31 Ga, 2.42 Ga and 2.22 Ga, respectively. The ages derived by Bugiolacchi and Guest (2008) were smaller than that of Hiesinger et al. (2000), especially for the northeastern and midwestern parts. Besides, due to the lack of orbiter hyperspectral data and corresponding analyzing methods, few previous studies had addressed the mineralogical variations of basalts within the Sinus Iridum, which are very important for constraining the compositional properties of magmatic activities in different geological period in this region.

Re-investigation of the geological features and the associated evolutionary history, especially the magmatic activities in the Sinus Iridum, with newly obtained remote sensing data could improve our understanding of the geologic facts in this region and provide additional scientific preparation for the future Chinese missions. Here we systematically study the topographic, compositional, stratigraphic and geological features in Sinus Iridum using new data, i.e., Lunar Reconnaissance Orbiter Altimeter (LOLA) and Camera (LROC), SELENE Terrain Camera (TC), Clementine ultraviolet–visible (UVVIS), and Chandrayaan-1 Moon Mineralogy Mapper ($M^3$) data. We discuss regional geological and magmatic evolution history, geochemical characteristics of mare basalts in Sinus Iridum, origin of olivine-rich rocks in this region, and propose two specific candidate landing sites for the future Chinese robotic and human exploration missions.

## 2. Regional geological setting

The Sinus Iridum region is centered at 45.01°N, 31.67°W. It has a diameter of 249 km (based on LOLA 2011 control network). The Sinus Iridum is surrounded by the Montes Jura from northeast to southwest (counterclockwise) and connects with Mare Imbrium by Promontorium Laplace at the northeastern cape and Promontorium Heraclides at the southwestern cape. Three large craters, i.e., Sharp, Bianchini and Maupertuis, are distributed in the northern and western highlands. The largest crater within the mare surface area of Sinus Iridum is the Laplace A crater (43.74°N,26.93°W, $D$=8 km, Fig. 1).

Previous research of Sinus Iridum mainly focused on the stratigraphy of mare basalts in this region. Schaber (1969) performed the earliest geologic mapping for the mare basalts based on the superposition and cross-cutting relations of the basalts using the Lunar Orbiter IV (90 m/pixel) and Lunar Orbiter V (7 m/pixel) photographs. Schaber (1969) divided the mare basalts within Sinus Iridum into three geological units, i.e., Im1, Im2 and EIm, in order of relative age from old to young. The Im1 and Im2 are later Imbrian stratigraphic unit, and the EIm is Eratosthenian and/or Imbrian stratigraphic unit and has a principal composition of mafic flows and/or ignimbrite deposits. Thus, stratigraphy analysis results indicated multiple magma filling events in Sinus Iridum with a time range from later Imbrian age to Eratosthenian age. The youngest units are small craters scattered on the surface of mare materials, including craters aged in Eratosthenian (unit Ec series) and Copernian (unit Cc series). There are also some large ray patches units and secondary impact crater chains (unit Ccsc), probably formed by ejecta from large crater of Copernian age, e.g., Copernicus, Aristillus and Aristarchus (Schaber, 1969).

Long-term magmatic activities, later tectonic movements and massive impact events had formed abundant geomorphic features within the Sinus Iridum, including sinuous rilles, wrinkle ridges, small craters and crater chains. Sinuous rilles mainly occur at the border between mare areas and the foot of Montes Jura, and they can be ~70 km long. Wrinkle ridges that have different morphologies are widely distributed within Sinus Iridum, especially in the joint region between Sinus Iridum and Mare Imbrium. Several wrinkle ridges are closely intertwined, and the can be ~200 km long. Impact craters in Sinus Iridum are all small bowl-shaped, with relatively simple structures and no central peaks.

## 3. Data and methods

### 3.1. Morphology analyses

To study the geomorphology of typical geomorphic features and proposed landing sites for the future Chinese missions, we used multiple imaging data sets, including those from the LROC Wide Angle Camera (WAC, 100 m/pixel), Narrow Angle Camera (NAC, 0.5–2 m/pixel), and the SELENE TC (~10 m/pixel)

(Haruyama et al., 2008; Robinson et al., 2010). The LROC WAC and SELENE TC images have been calibrated and geometric registered by the imaging teams, and the LROC NAC images are calibrated and registered using the USGS's Integrated Software for Imagers and Spectrometers (ISIS, http://isis.astrogeology.usgs.gov/). To better show the geomorphological features, we constructed some three-dimension (3-D) maps for specific regions using camera images and corresponding digit elevation model (DEM) composed by stereo-pair images, i.e., the LROC WAC GLD100 DTM (Scholten et al., 2011, 2012) and TC DTM data (Haruyama et al., 2012). 3-D maps based on imaging data and image-derived topography data can reduce the errors resulted by coregistering between multi-source data sets.

### 3.2. LOLA data and analyses

LOLA is a five-beams laser altimeter that operates at the 1064.4 nm wavelength with a 28-Hz pulse rate (Smith et al., 2010a, 2010b). The high vertical precision (10 cm), accuracy (~1 m) and density (~57 m along-track) of LOLA data provide unprecedented opportunity for detailed characterization of micro geomorphic features on lunar surface and also for landing site selection for future robotic and human exploration (Rosenburg et al., 2011). We established DEM for Sinus Iridum region using LOLA topography data, and made quantitative topographic analyses for this region (Figs. 1 and 2).

Surface slope and roughness are also crucial topographic parameters for the safety of lunar landing exploration. Surface slope is defined as the angle between the tangent plane across any point on the surface and the horizontal plane (Maune, 2007). We calculated the surface slope of Sinus Iridum in a $3 \times 3$ analysis windows using difference computation (Fig. 3) based on LOLA grid elevation data (Fig. 1). Surface roughness is defined as the topographic expression of surfaces at the horizontal scale (Shepard et al., 2001). There are many approaches for quantitative measurements of surface roughness, and residual standard deviation (RSD) altitude is one of the most commonly employed methods (e.g., Neumann et al., 2003). The RSD of altitudes between any measurement point on a planetary surface and the related baseline is calculated as the surface roughness. In this study, we used the 16 pixel/degree RSD roughness data derived by Smith et al. (2010b) to characterize the surface roughness of Sinus Iridum (Fig. 4). This roughness baseline varied from 30 to 120 m depending on the spacecraft altitude and orbital velocity of LRO, and the pixel values were interpolated using nearest-neighbor algorithm (Smith et al., 2010b).

### 3.3. Clementine UVVIS data and analyses

The Clementine UVVIS camera mapped the Moon at ultraviolet and visible wavelength in five spectral channels from 415 to

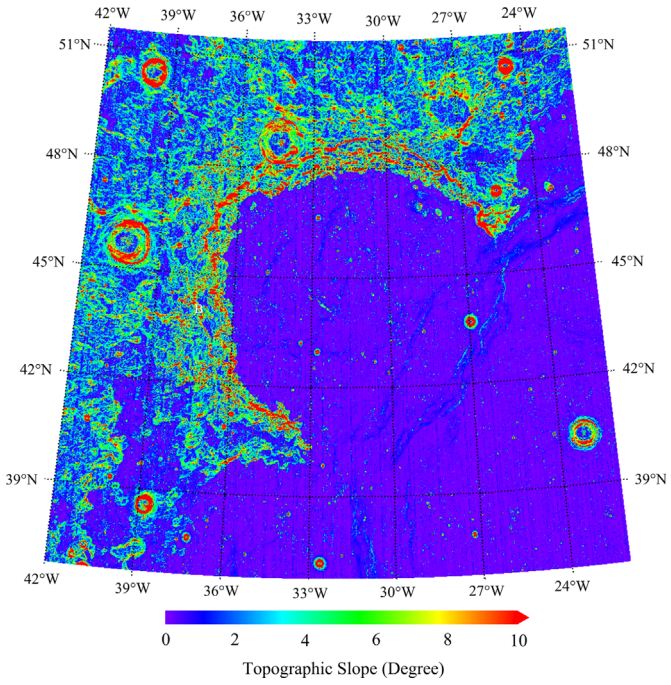



**Fig. 3.** Surface slope map of the Sinus Iridum based on LOLA topography data (Fig. 1). The map projection is Lambert conformal conic projection, the standard parallels are 42 °N and 47°N, and the central meridian is 32°W, up is the north.

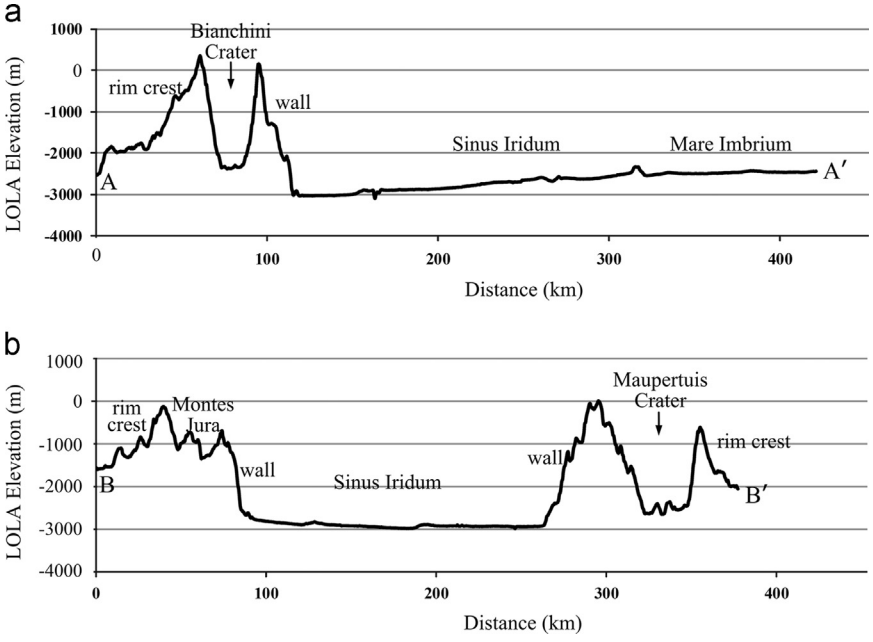



**Fig. 2.** Elevation profiles derived from LOLA topography data (Fig. 1). (a) Elevation profile from northwest to southeast (AA'), (b) Elevation profile from southwest to northeast (BB'). The arrows and labels mark the location of some typical landforms on the profiles, e.g., rim crest and crater wall.

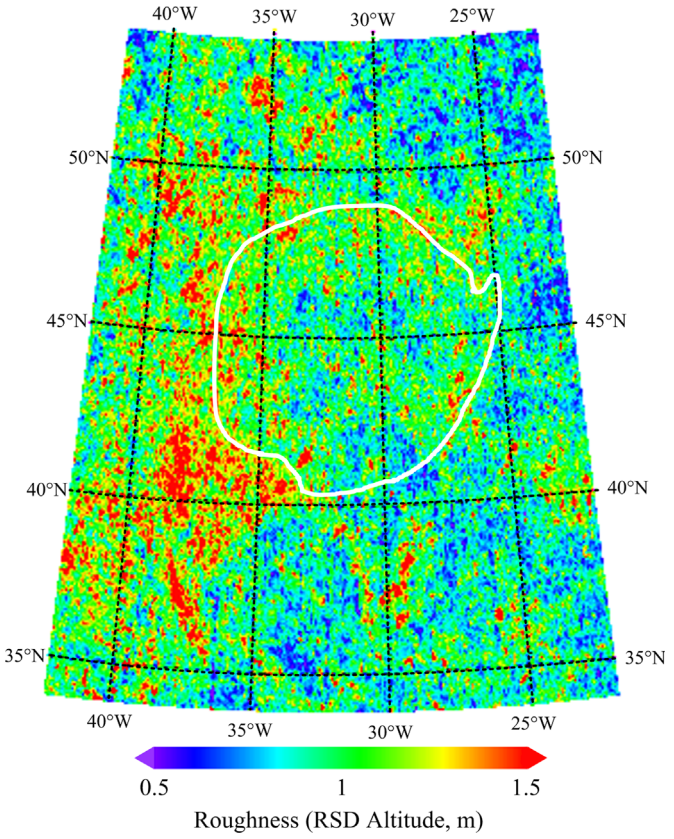



**Fig. 4.** Roughness map of the Sinus Iridum and surrounding areas (from Smith et al., 2010). The white curve represents the border of Sinus Iridum. The map projection is Lambert conformal conic projection, the standard parallels are 42°N and 47°N, and the central meridian is 32°W, up is the north.

1000 nm. The spatial resolution of UVVIS data is about 115 m/pixel (McEwen and Robinson, 1997; Nozette et al., 1994). The Clementine UVVIS data is available at the USGS Planetary GIS Web Server (http://webgis.wr.usgs.gov/). Global high spatial resolution imaging spectrometer data acquired by Clementine UVVIS camera provided powerful ways to estimate major element abundance of the lunar surface. Previous researchers had proposed several algorithms to determine the iron and titanium content (Gillis et al., 2003; Lucey et al., 1995, 1998, 2000). Here we use the algorithms proposed by Lucey et al. (2000) to calculate the FeO and $TiO_2$ abundance in Sinus Iridum (Fig. 5). The algorithms are defined as:

$$\mathrm{FeO\ (wt\%)} = 17.427 \times \arctan((R_{950}/R_{750} - 1.19)/(R_{750} - 0.08)) - 7.565 \quad (1)$$

$$\mathrm{TiO_2(wt\%)} = 3.708 \times (\arctan(R_{415}/R_{750} - 0.42)/R_{750})^{5.979} \quad (2)$$

where $R_\lambda$ is the reflectance value at a given wavelength $\lambda$ ($\lambda$=415, 750 or 950 nm). The Lucey algorithms have standard deviations of 1.29 wt% for FeO and 0.93 wt% for $TiO_2$ (Lucey et al., 2000).

### 3.4. $M^3$ data and analyses

$M^3$ is a push-broom imaging spectrometer onboard India's Chandrayaan-1 spacecraft. It operates at continuous spectra from 0.43 to 3.0 μm to effectively detect the absorption features of lunar major rock-formation minerals (Pieters et al., 2009). The actual $M^3$ observations are operated during several optical periods depending on the orbit altitude of Chandrayaan-1, phase angles and star sensors (Boardman et al., 2011). The Optical Period 2C (OP2C) measurements covered the entire Sinus Iridum region and therefore were used in this study. During the OP2C observations, the $M^3$ spectrometer mapped the lunar surface at 280 m/pixel in 85 spectral channels (Pieters et al., 2009).

The $M^3$ team has developed a series of mineral indicator parameters to characterize the fundamental mineralogical properties (e.g., mafic silicates, soil maturity, and space weathering) of lunar surfaces. The integrated band depth (IBD) of the crystal field absorptions at 1 and 2 μm and the reflectance measured at 1.58 μm can effectively reflect the mineral diversity of the surface using $M^3$ data (Mustard et al., 2011). The algorithms of the integrated band depth for the 1 μm (IBD (1 μm)) and 2 μm (IBD (2 μm)) are defined as:

$$\mathrm{IBD(1\ \mu m)} = \sum_{n=0}^{26}\left(1 - \frac{R(789+20n)}{Rc(789+20n)}\right) \quad (3)$$

$$\mathrm{IBD(2\ \mu m)} = \sum_{n=0}^{21}\left(1 - \frac{R(1658+40n)}{Rc(1658+40n)}\right) \quad (4)$$

where $R$ is the reflectance at a given wavelength, $Rc$ refers to the continuum reflectance value (continuum is defined as a slope line across the absorption band), 789 and 1658 are the starting wavelength in nanometer, 20 and 40 are the spectral sampling interval in nanometer, and $n$ is the number of bands to be covered by the absorption features (Cheek et al., 2011; Mustard et al., 2011). We made the composite spectral parameters map for the Sinus Iridum region (Fig. 6).

## 4. Results

### 4.1. Topography of Sinus Iridum

From the LOLA topography map (Fig. 1), the Sinus Iridum and Mare Imbrium have similar elevations and comparable flat topography. Compared with the surrounding Montes Jura that features an average elevation of above −2000 m, Sinus Iridum shows an apparent topographic depression, in which most areas have elevations of between −3000 m and −2000 m. Whereas inside the Sinus Iridum region, the terrain shows a falling trend from the southeast (border to Mare Imbrium) to the northwest (near to Montes Jura). The NW-SE elevation profile (Fig. 2a) shows that the elevation decreases from about −2500 m at the southeast to below −3000 m at the northeast, with a total elevation decrease of ~500 m. The rim crests and the center peaks of crater Bianchini and Maupertuis can be also recognized from the elevation profiles (Figs. 1 and 2).

The topographic slope map shows that most areas in Sinus Iridum and Mare Imbrium are flat, and the slope is less than one degree for over eighty percent of the inner Sinus Iridum mare surface. On the walls of some craters, e.g., the northern wall of Laplace A crater, the topography slope can be greater than 20°. The surface roughness of most areas within Sinus Iridum is low. The RSD altitude roughness for over ninety percent of the inner Sinus Iridum region is lower than 1.3 m, indicating that there are generally few discrete positive relief features, such as large-scale outcrops or large boulders ( > 2 m diameter), in the region.

### 4.2. Iron and titanium abundance of mare basalts within Sinus Iridum

Major elements compositions are important indicators of regional geological features and thus are essential for landing site selection for lunar landing exploration missions. The iron and titanium content maps (Fig. 5) show that the FeO contents in the Sinus Iridum and Mare Imbrium are much higher than the surrounding highland regions. About ninety-five percent of the

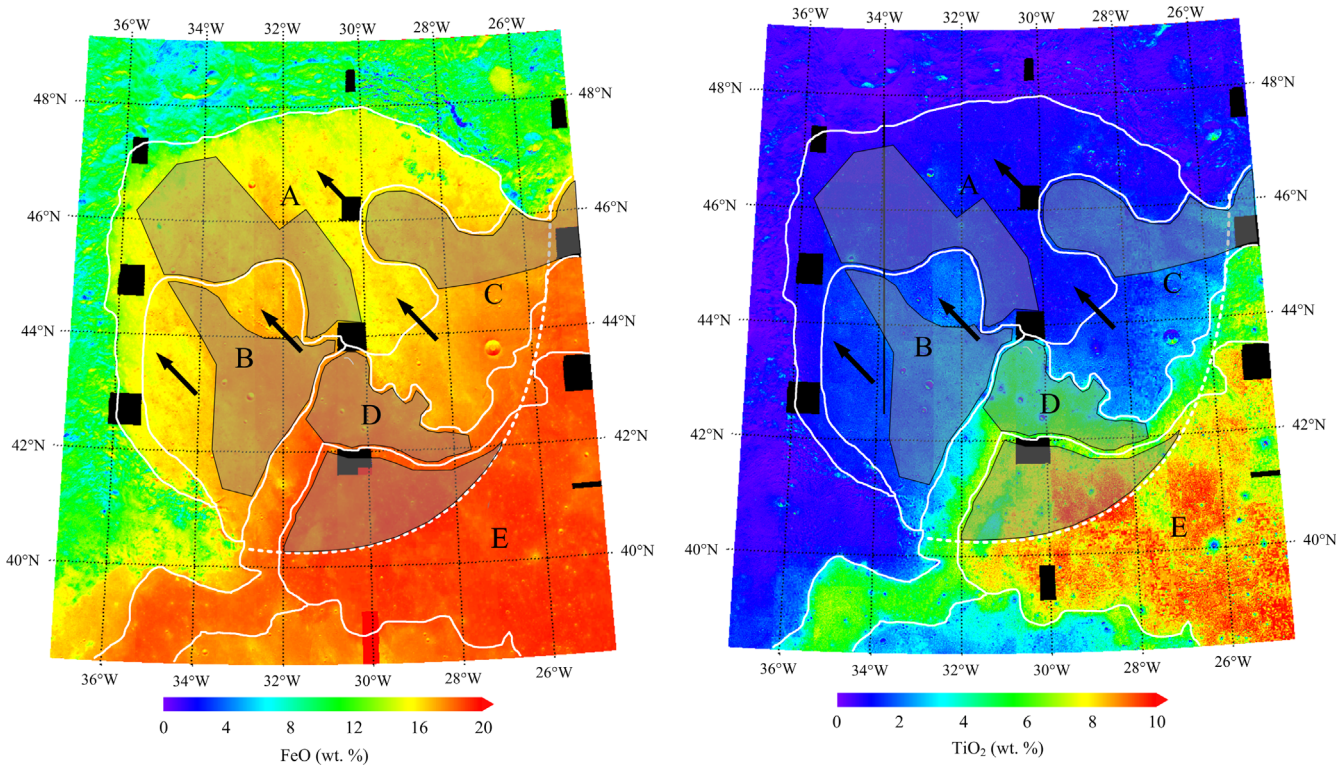



**Fig. 5.** FeO (left) and $TiO_2$ (right) contents of Sinus Iridum based on Clementine UVVIS data. The black blocks are missing value areas, the white curves outline compositional homogeneous units defined for Sinus Iridum and northwest Mare Imbrium, the black arrows mark secondary craters concentration areas, and crater size-frequency distribution measurements were performed for the areas highlighted in dark gray. The map projection is Lambert conformal projection, the standard parallels are 42°N and 47°N, the central meridian is 32°W, and up is the north.

inner Sinus Iridum area has a FeO content from 14 wt% to 20 wt%, with a mean content of 15.3 wt%. While the $TiO_2$ contents of the northern Sinus Iridum and the surrounding highland are much lower than those of basalts in Mare Imbrium. About ninety percent of the inner Sinus Iridum area has a $TiO_2$ content lower than 5 wt%, with a mean content of 1.9 wt%. The northwestern Mare Imbrium is characterized as a relatively high-titanium basaltic area, with a $TiO_2$ content of nearly 10 wt% on average. Our results of the FeO and $TiO_2$ contents within the Sinus Iridum region are consistent with those of Bugiolacchi and Guest (2008). Chen et al. (2010) suggested that the inner Sinus Iridum region and surrounding highlands are high-iron and medium-titanium, and the Mare Imbrium region is low-iron and high-titanium where the maximum $TiO_2$ content can be over than 25 wt%. However, both global remote sensing data (e.g., Lucey et al., 1998; Wu et al., 2012) and returned samples data (e.g., Papike et al., 1976) indicate that the mare basalts are more iron-rich than the highland materials and the maximum $TiO_2$ content of lunar materials is about 14 wt%. This suggests that our results are consistent with previous global remote sensing results and lunar samples data. The iron and titanium contents also show regional variations in both Sinus Iridum and northwestern Mare Imbrium, indicating compositional diversity of different magmatic activities.

### 4.3. Mineralogy within the Sinus Iridum

The 1 μm and 2 μm absorption features shown in the $M^3$ data can display the distribution of lunar major rock-formation minerals in the Sinus Iridum region. Previous remote sensing detection suggested that there are three major minerals on lunar surface, i.e., plagioclase, pyroxene, and olivine (Adams, 1974; Adams and Goullaud, 1978). Pyroxene has strong absorption bands at both 1 μm and 2 μm, and thus is yellowish green in the spectral parameter map. Olivine has a strong 1 μm absorption band but weak 2 μm absorption band, and therefore appears reddish in the spectral parameter map. Plagioclase lacks any distinctive iron-related absorption bands and appears as bluish in the spectral parameter map (Mustard et al., 2011).

The composite spectral parameter map of the Sinus Iridum region clearly distinguishes the mare areas from the surrounding highlands. The materials in the Sinus Iridum and northwestern Mare Imbrium (e.g., point a in Fig. 6) display relatively weak absorption features at both 1 μm and 2 μm (Fig. 7a), indicating that pyroxene is the dominated mineral. The relatively weak absorption features are probably caused by the long-term space weathering (Pieters et al., 1993). By comparison, some fresh pyroxene-rich materials are visible at the western wall of the Laplace A craters (point b in Fig. 6), of which the $M^3$ spectrum displays strong absorptions at both 1 μm and 2 μm (Fig. 7b). The materials in the surrounding highlands (point c in Fig. 6) generally lack the two iron-related absorption bands (Fig. 7c) and thus appear much brighter in the reflectance image, suggesting a feldspar-dominated composition. Additionally, in the northern wall of Sinus Iridum (point d in Fig. 6), some olivine-rich materials are visible that feature a strong absorption band at 1 μm but a weak to absence 2 μm band (Fig. 7d). Besides, materials within the inner Sinus Iridum show regional variations in mineralogy as the composite map (Fig. 6) changes from yellowish-green in the north to reddish yellow in the south, indicating a gradual increase of olivine abundance.

### 4.4. Geomorphology of wrinkle ridges and sinuous rilles in Sinus Iridum

#### 4.4.1. Winkle ridges in Sinus Iridum

Wrinkle ridges are linear and uplifted structures concentrated in, but not limited, the mare regions. Wrinkle ridges are typically consisted of two separate but related parts. The lower is a board and gentle arch, and the upper is a shaper, steeper, and more

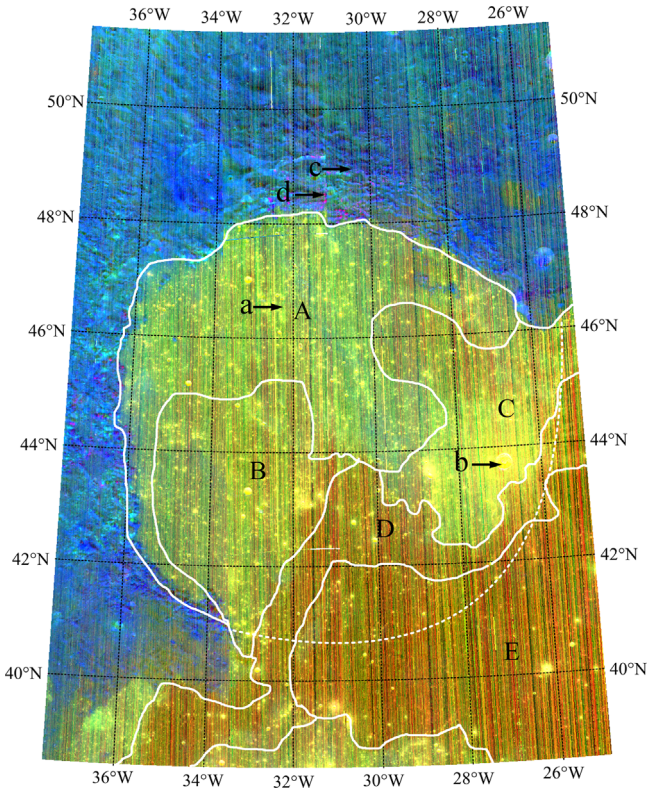



**Fig. 6.** Composite map of spectral parameters in the Sinus Iridum calculated from $M^3$ data. Red is the integrated band depth (IBD) at 1 μm, green is the IBD at 2 μm, and blue is the apparent reflectance at 1.58 μm. The white solid lines demarcate the boundaries of geological units defined based on chemical composition in Section 5, and the black arrows indicate the location of some materials of typical mineral composition, of which spectra are displayed in Fig. 7. The map projection is Lambert conformal projection, the standard parallels are 42°N and 47°N, the central meridian is 32°W, and up is the north. (For interpretation of the references to color in this figure legend, the reader is referred to the web version of this article.).

twisted ridge (Strom, 1972). The lunar wrinkle ridges occurring in mare region were generally believed to be purely tectonic landforms, which originated from basin-localized folding and faulting over thrust faults (e.g., Maxwell, 1978; Golombek et al., 1991; Watters, 2004). Several wrinkle ridges are visible within the Sinus Iridum region, of which parts are closely intertwined with each other and have a generally northeast-southwest or north–south direction trending. The ridge in the connecting region of Sinus Iridum and Mare Imbrium, is the longest in this area (Fig. 8a). This ridge extends over 200 km along the southeastern border of Sinus Iridum. On the elevation profile that transects this ridge (Fig. 8b), this ridge is nearly 13 km wide at the bottom and can be clearly identified as the lower gentle arches (the B–C and E–F parts shown in Fig. 8b) and upper steeper ridge (the C–D–E part in Fig. 8b). The lower arches are about 5.5 km wide at both sides (B–C = 5.6 km, E–F = 5.4 km), and the western side (B–C part) is relatively gentle with a mean slope of about 10°, and the eastern side (E–F part) is steeper with a mean slope of about 17°. The upper ridge part is relatively narrow (C–D–E = 1.72 km) and much steeper (mean slope over 40°). The top of the ridge (point D in Fig. 8b) shows an elevation uplift of over 200 m from the mare surface (point F in Fig. 8b).

#### 4.4.2. Sinuous rilles

Lunar sinuous rilles are winding, channel-like features on the lunar surface (Hulme, 1982). The longest sinuous rille in this region is located at the northeastern Sinus Iridum (Fig. 9). This rille originates from an irregular crater (point H in Fig. 9) that is about 25 km to the east of Promontorium Laplace. After buried by a chain of small craters, the rille extends westward and passes by the Promontorium Laplace. The rille continues northwestward, faded at the foot of Montes Jura, and eventually terminates indistinctly in a small crater (point A in Fig. 9). This rille is about 70 km long, 100–500 m wide, and 0.5–10 m deep. It can be divided into two parts at the two sides of Promontorium Laplace as the west linear part and the east sinuous part. The west linear part is rarely cut or buried by craters and ridges, except for being partially buried by mass wasting deposits from the wall (point B in Fig. 9; Xiao et al., 2013). While the east sinuous part is cross-cut several times by wrinkle ridges (e.g., points C and E in Fig. 9) and shows elevated rims when encountering the ridges.

A recent study of the origination of the lunar sinuous rilles suggested that thermal erosion was likely the dominated factor in the formation of sinuous rilles when lava flowed over a gradually sloping (i.e., $<3.5^{\circ}$) surface of cooled lava plain (Hurwitz et al., 2012). Hurwitz et al. (2013) made a global survey of lunar sinuous rilles, including the sinuous rille in this study, and indicated that it was formed as the result of lava erosion into the mare surface and the surrounding mare surface age (3.21 Ga in Section 5) represented an upper age limit of formation of this sinuous rille. The superposition and cross-cutting relations of the wrinkle ridges and sinuous rille suggest that these wrinkle ridges postdated the sinuous rille. The superposition relationships essentially confirm the stratigraphic units definition and surface dating results in this study (Section 5). The wrinkle ridges also pass through the youngest geological unit in northwestern Mare Imbrium, indicating that wrinkle ridges represent the last stage of regional tectonic evolution within the Sinus Iridum.

## 5. Model ages and thickness of mare basalts in Sinus Iridum

We investigated the surface model ages of mare basalts within Sinus Iridum and northwestern Mare Imbrium using crater size-frequency distribution (CSFD) method. The detailed method was explained in Michael and Neukum (2010). We also estimated the thickness of each basalt unit based on method suggested by Thomson et al. (2009).

### 5.1. Definition of Mare units

The mare surfaces in Sinus Iridum may have experienced different magmatic activities, resulting in the observed compositional variations (Fig. 5). It is essential to define compositionally homogeneous units in order to obtain reliable surface ages. Previous researchers used band ratios, albedo variations or surface texture changes to distinguish homogeneous areas (e.g., Hiesinger et al., 2000), while these methods had some subjective factors and they could not define the quantitative chemical variations between different units. Iron and titanium contents are major component of mare basalts and have been used as makers to classify mare basalts (e.g., Kaula et al., 1981; Papike et al., 1976). We use iron and titanium content variations (calculated in Section 3.3) to define compositional homogeneous units in Sinus Iridum. According to geographical continuity and specified FeO and $TiO_2$ content thresholds (Table 1), we defined five homogeneous units in the Sinus Iridum and northwestern Mare Imbrium region. The boundaries of the five homogeneous units are showed in Fig. 5. The mean FeO and $TiO_2$ contents for each unit are calculated in Table 1.

### 5.2. Crater count statistics and surface model ages of mare units in Sinus Iridum

We used the LROC WAC 100 m/pixel mosaic images (http://www.lroc.asu.edu/, Robinson et al., 2010) to count craters in the

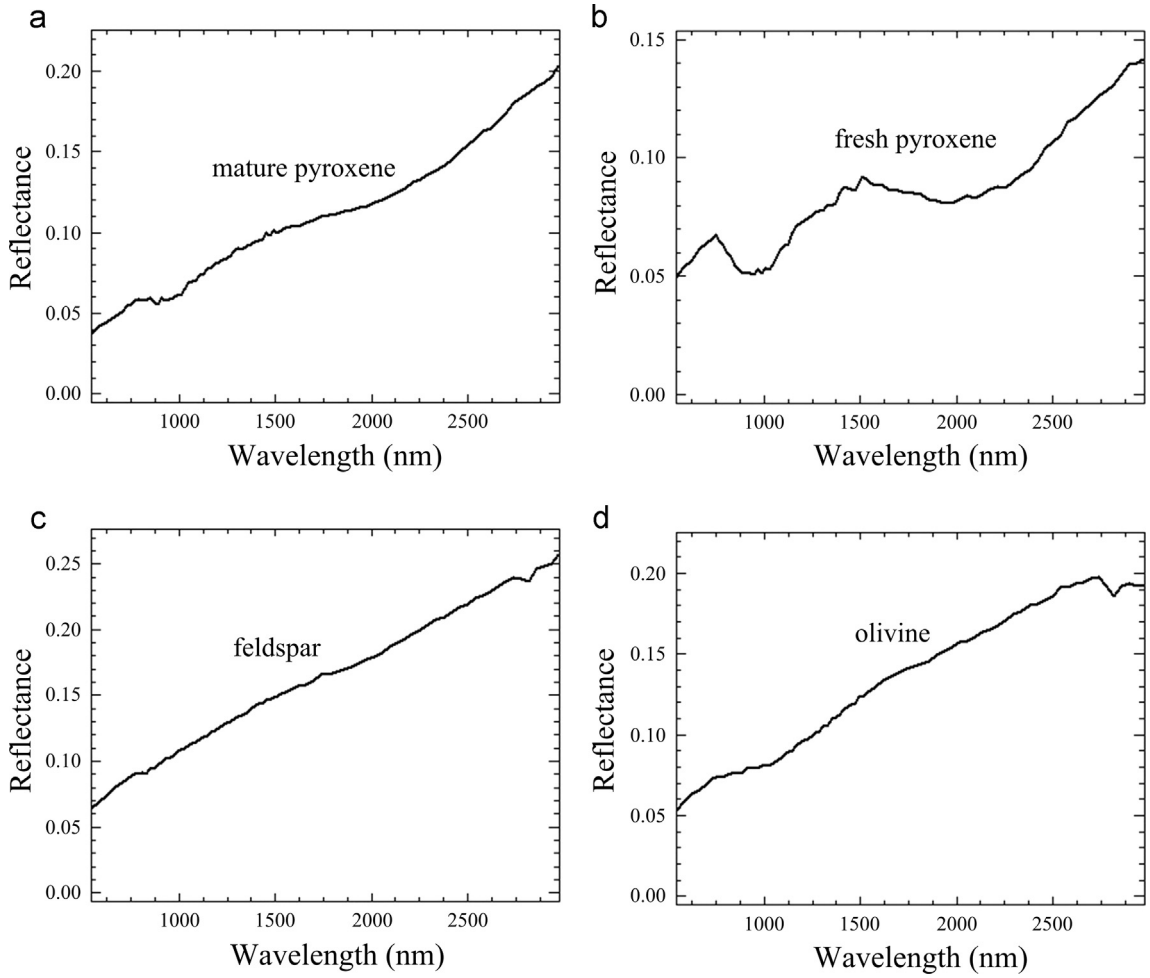



**Fig. 7.** Spectra of four typical materials in the Sinus Iridum basin and surrounding areas. (a) mature pyroxene-rich basalt in Sinus Iridum, (b) fresh pyroxene-rich rocks at the wall of fresh impact craters, (c) feldspathic materials on the surrounding highlands, (d) olivine-rich rocks in the north crater wall of Sinus Iridum, near the Montes Jura.

five sub-mare units in Sinus Iridum and northwestern Mare Imbrium. The WAC mosaic images have relatively larger incidence angles (53–70°) to support reliable morphologic interpretations of lunar surface features (Kirchoff et al., 2013; Robinson et al., 2010) and therefore are better than images returned by the Lunar Orbiter missions, that were used in the previous researches. The WAC mosaics are map-projected in a Lambert conformal projection because this projection causes little distortion in mid-latitudes areas (Snyder, 1987).

We chosed several relatively flat mare areas in the five units to conduct the crater counts. The areas near the Montes Jura were avoided because they appeared to be covered by materials collapsed from the wall (Xiao et al., 2013). CSFD measurements are easily polluted by secondary craters towards small diameters (Xiao and Strom, 2012). In this study, we tried to eliminate the secondaries problem in three ways: (1) We excluded areas clearly affected by secondary craters (e.g., clusters and/or chains of small craters, etc.) to reduce the work for recognizing secondary craters, as marked in Fig. 5. (2) We only counted impact craters with diameter greater than 500 m because small craters may have been saturated and contain more secondary craters (Xiao and Strom, 2012). (3) During the CSFD measurements, we avoided possible secondary craters based on their morphological characteristics (e.g., irregular craters, chain craters and clusters; Melosh, 1989).

We used the Neukum crater production and chronology functions (PF and CF; Neukum et al., 2001) to fit the observed CSFD measurements and to calculate the model ages. Errors of the estimated ages are determined by log $(N+N^{1/2})/A$, where $A$ is the size of the counting area and $N$ is the cumulative number of craters (Arvidson et al., 1979). In this study, the software "craterstats" (http://hrscview.fu-berlin.de/software.html; Michael and Neukum, 2010) were employed to derived model ages and their errors from CSFD measurements.

We obtained model ages for the five geological units (Fig. 10) and specified the stratigraphic name for each unit (Table 2). The Im1 and Im2 are Imbrian mare stratigraphic units and Im1 is older than Im2, and the Em1 and Em2 are Eratosthenian mare stratigraphic units and Em1 is older than Em2. Moreover, the chemical composition and model ages of the western (unit B in Fig. 5) and northeastern (unit C in Fig. 5) units are very close with each other, indicating that the basalts in these two units were filled by the same magmatic activity. The similar model ages and chemical composition of these two units are consistent with the stratigraphic units definition by Schaber (1969) and the latest surface dating results (Zhao et al., 2013), and partly proved the validity of our CSFD measurements. Additionally, we should be aware of the similar chemical composition and model ages of unit A and B/C, the difference of FeO, $TiO_2$ contents and model ages between unit A and B/C are near to the inherent uncertainty of the relevant algorithms (1.29 wt% for FeO, 0.93 wt% for $TiO_2$, $+0.06/-0.08$ Ga, $+0.07/-0.11$ Ga and $+0.09/-0.15$ Ga for model ages of unit A, B and C). While we suggest to distinguish unit A from unit B/C because we can still find the relatively visible hue boundaries between unit A and B/C on the $TiO_2$ content map (Fig. 5), as

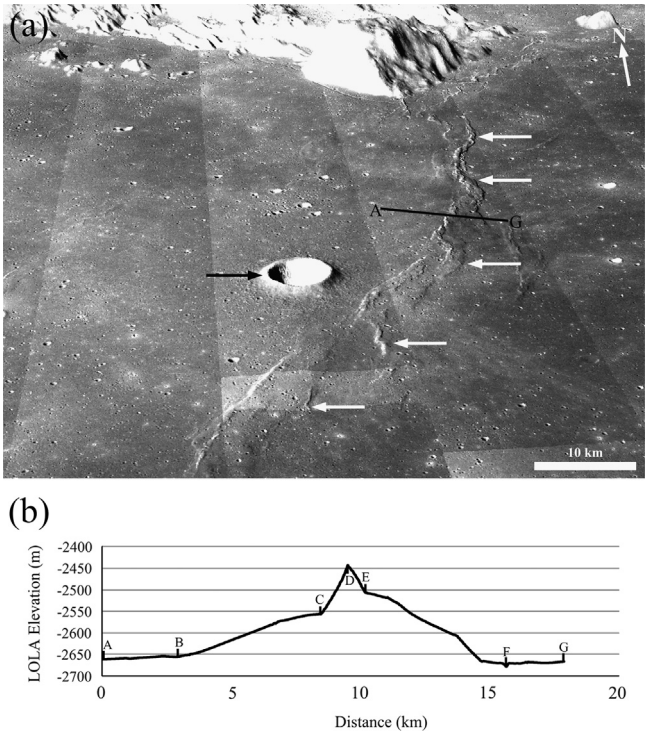



**Fig. 8.** The longest wrinkle ridge in southeast Sinus Iridum, border to Mare Imbrium. (a) 3-D view of the ridge, with LROC WAC mosaic (Lambert conformal projection centered at 44.13°N, 26.40°W) overlying GLD100 topography data (100 m/pixel). The map scale is only true along its direction and the vertical exaggeration factor is 2.5. The white arrows point the location and trend of the ridge, black arrow points to the Laplace A crater, the black line shows the location of elevation profile derived from LOLA topography (Fig. 8 b). (b) Elevation profile across-cut the ridge from east to west (LOLA topography data, 1024 pixel/degree). Major elevation turning points are labeled with letters, the B–C and E–F parts are the lower board and gentle arch, C–D–E part is the upper shaper, steeper and twisted ridge structure.

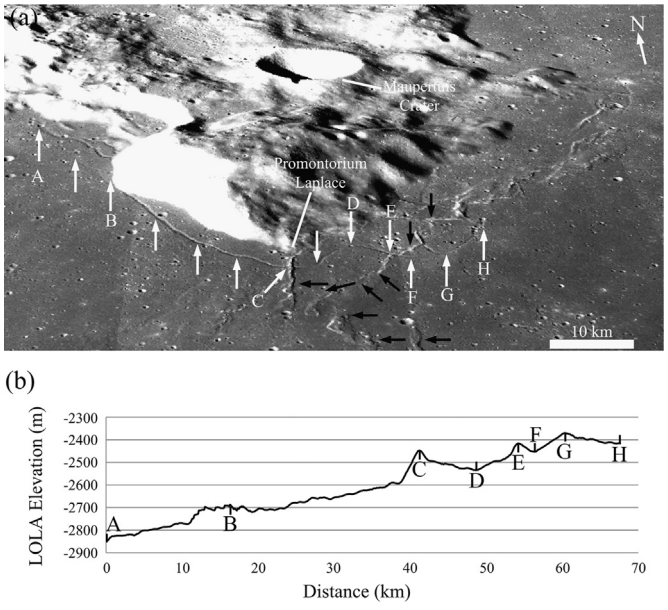



**Fig. 9.** The longest sinuous rille in northeast Sinus Iridum. (a) 3-D view of the sinuous rille, with LROC WAC mosaic (Lambert conformal projection centered at 45.88°N, 25.76°W) overlying GLD100 topography data (100 m/pixel). The map scale is only true along its direction and the vertical exaggeration factor is 1.5. (b) Elevation profile along the rille. The white arrows point to the path of the rille, the black arrows point to the cross-cutting wrinkle ridges, and the letters label major elevation turning points along the rille.

**Table 1**
FeO and $TiO_2$ content thresholds for defining homogeneous units in the Sinus Iridum and northwestern Mare Imbrium region, and the mean chemical content of each unit and the inner Sinus Iridum region. The standard deviations are 1.29 wt% for FeO content and 0.93 wt% for $TiO_2$ content (Lucey et al., 2000).

| | Sinus Iridum | A | B | C | D | E |
|---|---|---|---|---|---|---|
| Mean FeO content | 15.3 | 15.1 | 16.3 | 16.5 | 17.6 | 18.3 |
| Lower FeO threshold | | 12.8 | 15.1 | 15.4 | 16.9 | 17.7 |
| Upper FeO threshold | | 16.2 | 17.2 | 17.2 | 18.1 | 18.7 |
| Mean $TiO_2$ content | 1.9 | 1.1 | 1.8 | 1.9 | 4.9 | 7.9 |
| Lower $TiO_2$ threshold | | 0.5 | 1.2 | 1.2 | 2.7 | 5.8 |
| Upper $TiO_2$ threshold | | 1.5 | 2.6 | 2.8 | 6.7 | 9.5 |

previous research of mare basalts in Mare Imbrium region (Bugiolacchi and Guest, 2008). We compared our model ages with previous results (Table 2; Bugiolacchi and Guest, 2008; Hiesinger et al., 2000; Morota et al., 2011; Schaber, 1969; Zhao et al., 2013). Our results are relatively consistent with those of Hiesinger et al. (2000), both in terms of spectral units definition and model ages determination, even there are differences in details (Fig. 11). We have defined a new mare unit (Em1) comparing with the Hiesinger et al. (2000). For all the five units defined in this study, the age differences between our ages and those of Hiesinger et al. (2000) are less than 0.5 Ga.

### 5.3. Thickness of mare basalts in Sinus Iridum

Numerous small craters are superposed on the northwestern mare surface of Mare Imbrium (unit Em2). These craters have different diameters, excavation depths and compositions of the ejecta. Some larger craters may have penetrated the whole basaltic layer and excavated subsurface primitive highland materials. While some small craters may have excavated very shallow lavas and only penetrated part of the top basaltic stratum (Em2). From the excavation depths and ejecta' $TiO_2$ contents of these craters, we could infer the coverage relationship of these strata and estimate the thickness for each basaltic stratum in this region (Thomson et al., 2009). We selected several representative craters and judged the original strata of impact ejecta before the excavation by comparing their $TiO_2$ content with threshold contents to define homogeneous units (Section 5.3). We measured the rim-to-rim diameter of these craters, and calculated the excavation depths accordingly (Table 3) since the excavation depths scale with diameters (0.084:1 for simple craters; Melosh, 1989; Thomson et al., 2009). According to typical principle of strata superposition, i.e., older on the lower and younger on the upper (e.g., van Gasselt and Nass, 2014), we suggested that the excavation depth of a crater is not greater than the depth of the bottom of the stratum where the ejecta came from, but greater than that of the upper and younger stratum. Table 3 lists the excavation depth of each crater measured in this study. It can be concluded that the depths of the bottom of stratum Im1, Im2, Em1, Em2 are from 203 to 216 m (estimated as 210 m), 103 to 105 m (estimated as 104 m), 41 to 73 m (estimated as 55 m), and 14 to 21 m (estimated as 17 m) respectively. The thickness of each stratum can be then calculated as the bottom depth difference between two adjacent strata, i.e., 106 m, 49 m, 38 m and 17 m for Im1, Im2, Im3 and Im4 respectively, indicating that the volume of lava erupted by different magmatic activities declined with time.

## 6. Discussion

### 6.1. Magmatic evolution history in Sinus Iridum

Compositional variation of mare basalts is a direct indication of the nature and evolution of magma source regions. The correlation

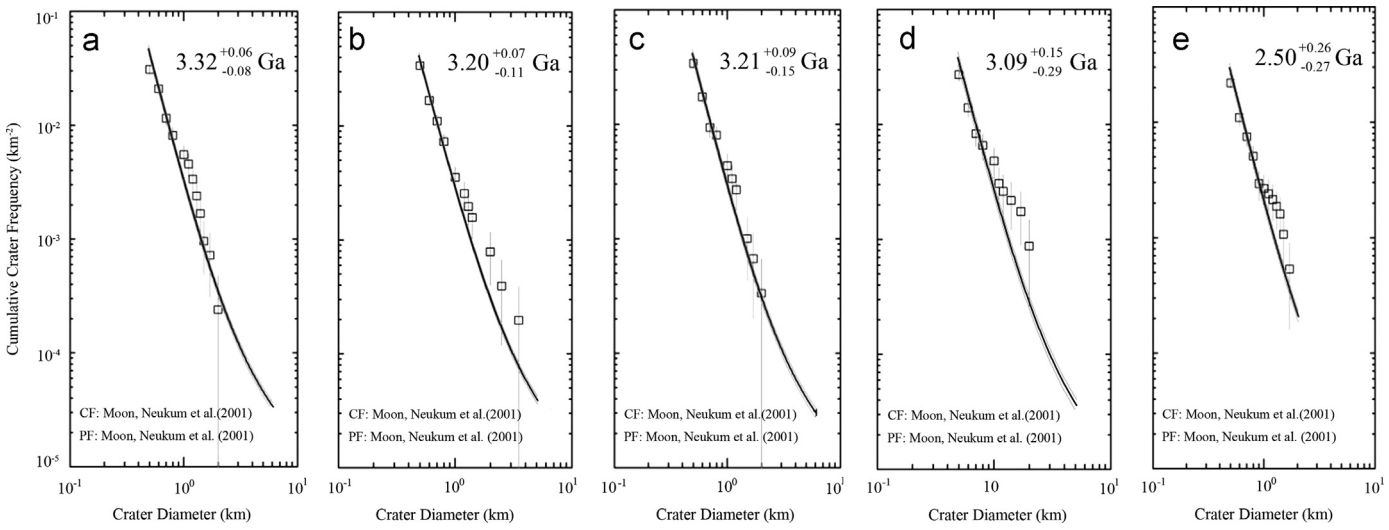



**Fig. 10.** Cumulative crater size-frequency distributions and derived model ages of each homogeneous unit. Black curves indicate the crater production function (PF, Neukum et al., 2001) fitted to the observed CSFD measurements.

**Table 2**
Model ages for lava flows in the Sinus Iridum and northwestern Mare Imbrium.

| Units | Area (km$^2$) | Surface Age (Ga) | Error (Ga) | Stratigraphy (this paper) | Hiesinger (2000) | Schaber (1969) | Bugiolacchi (2008) | Morota (2011) | Zhao (2013) |
|---|---|---|---|---|---|---|---|---|---|
| **A** | 15021 | 3.32 | +0.06/−0.08 | Im1 | 3.26 | Im1/Im2 | 3.31 | | 3.33 |
| **B** | 9069 | 3.20 | +0.07/−0.11 | Im2 | 3.01 | Im1/Im2 | 2.42 | | 3.21 |
| **C** | 6588 | 3.21 | +0.09/−0.15 | Im2 | 3.39 | Im1/Im2 | 2.42/3.31 | | 3.21 |
| **D** | 72312 | 3.09 | +0.15/−0.29 | Em1 | 3.26/2.96 | Im1/Elm | 2.42 | | 2.60 |
| **E** | 15861 | 2.50 | +0.26/−0.27 | Em2 | 2.96 | Elm | 2.22 | 2.29 | 2.60 |

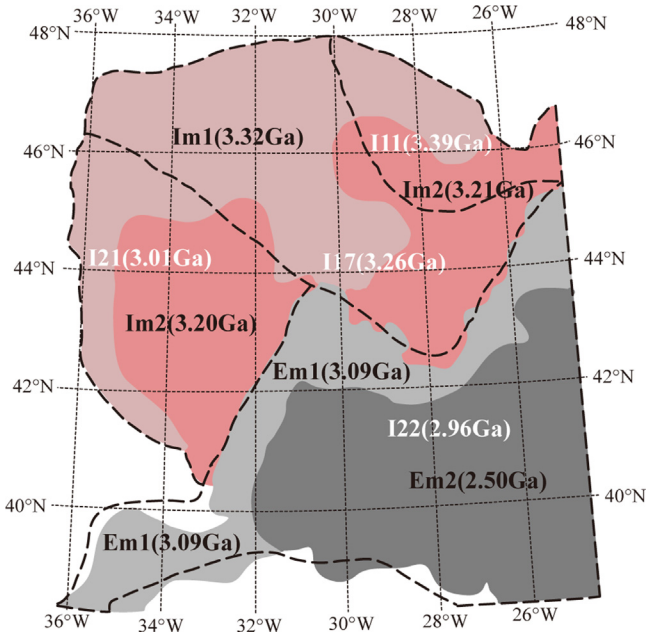



**Fig. 11.** Comparation of the mare units definition and model ages determination of this study with those of the Hiesinger et al. (2000). The filled areas represent the mare units defined in this study, and black letters (Im1, Im2, Em1 and Em2) label their names and derived model ages. The dashed lines represent the boundaries of spectral units defined by Hiesinger et al. (2000), and the white letters (I11, I17, I21 and I22) label their names and derived model ages.

between titanium contents and ages of mare basalts has been previously reported. Laboratory analyses of returned lunar samples suggest that old basalts generally contain higher titanium content than young basalts (e.g., Taylor et al., 1991). But the returned lunar samples are only collected in several limited areas, and do not represent the whole Moon. Global remote sensing data (e.g., Clementine UVVIS) reveals that mare basalts collected by Apollo and Luna missions are generally very old and no such simple correlation exists between the titanium contents and ages of mare basalts (e.g., Hiesinger et al., 1998). However it was also reported that this chemical–temporal trend existed within local geological settings in the "Procellarum KREEP Terrane" (PKT; e.g., Bugiolacchi and Guest, 2008; Morota et al., 2011). This study also reveals a high correlation between the titanium contents and ages of mare basalts in the Sinus Iridum and northwestern Mare Imbrium region, which is consistent with previous results (Bugiolacchi and Guest, 2008; Morota et al., 2011). Basalts filled by the earlier Imbrian-age magmatic activities (Im1 and Im2) in the northern Sinus Iridum contain more titanium than those formed by the later Eratosthenian-aged magmatic activities (Em1 and Em2 ) in the southern Sinus Iridum and northwestern Mare Imbrium. Even considering the possibility that Em1 (unit A) and Em2 (unit B/C) are treated as one single mare unit, this composition-age correlation still remains valid. This relationship suggests that magmatic activities in Sinus Iridum have evolved from low-titanium to medium-titanium with time.

Moreover, the mineral composition of mare basalts also shows a well correlation with their ages. The younger Eratosthenian-aged basalts (Em1 and Em2) within the southern Sinus Iridum and northwestern Mare Imbrium are more olivine-rich than the older Imbrian-aged basalts within the northern Sinus Iridum. It has been reported that the last major phases of lunar volcanism produced unique high-titanium and high-olivine basalts on the western nearside of the Moon, including the southern Sinus Iridum and northwestern of Mare Imbrium in this study (e.g., Staid et al., 2011).

**Table 3**
Excavation depths and titanium contents of craters in northwestern Mare Imbrium (unit Em2).

| No. | Lat (°N) | Lon (°W) | Diameter (km) | Excavation depth (m) | $TiO_2$ of the surrounding materials (stratigraphy) | $TiO_2$ of the deepest ejecta materials (stratigraphy) | Comments[a] |
|---|---|---|---|---|---|---|---|
| **1** | 40.46 | 25.66 | 2.43 | 204 | 7.8 (Em2) | 1.1 (Im1) | $H_{Im1} \geq 203m > H_{Im2}$ |
| **2** | 41.75 | 24.92 | 2.57 | 216 | 7.2 (Em2) | 0.3 (Highland) | $216m > H_{Im1}$ |
| **3** | 40.19 | 24.85 | 1.22 | 103 | 8.6 (Em2) | 2.5 (Im2) | $H_{Im2} \geq 103m > H_{Em1}$ |
| **4** | 38.46 | 26.25 | 1.25 | 105 | 7.5 (Em2) | 1.3 (Im1) | $H_{Im1} \geq 105m > H_{Im2}$ |
| **5** | 39.86 | 27.72 | 0.49 | 41 | 8.8 (Em2) | 4.4 (Em1) | $H_{Em1} \geq 41m$ |
| **6** | 40.37 | 24.87 | 0.87 | 73 | 8.1 (Em2) | 2.9 (Im2) | $H_{Im2} \geq 73m > H_{Em1}$ |
| **7** | 39.35 | 24.88 | 0.16 | 14 | 8.9 (Em2) | 7.1 (Em2) | $H_{Em2} \geq 14m$ |
| **8** | 39.88 | 27.34 | 0.25 | 21 | 8.3 (Em2) | 5.9 (Em1) | $21m > H_{Em2}$ |

[a] $H_X$=Depth of the bottom of unit X, X=Im1, Im2, Em1 or Em2.

The good correlation between composition and ages of mare basalts suggests that this region has experienced complex magmatic activities and future in-situ quantitative composition analyses may get important constraints on the lunar late-stage volcanism and thermal evolution history.

### 6.2. Geochemical characteristics of mare basalts in Sinus Iridum

Analyses of returned lunar samples indicate the large variations in the $TiO_2$ contents of lunar mare basalts, determined by both their magma source and subsequent differentiation processes. The $TiO_2$ contents of lunar basalts vary from about 0.5 wt% to about 14 wt% (e.g., Kaula et al., 1981). Mare basalts can thus be classified as high-titanium and low-titanium series according to their $TiO_2$ contents, and then further subdivided into several subgroups according to other chemical parameters (e.g., Papike et al., 1976). Fig. 12 shows the FeO and $TiO_2$ contents of all typical kinds of lunar basalts. There is a bimodal abundance distribution for $TiO_2$ contents of mare basalts with a distinct gap between the high-titanium and low-titanium basalts. But global remote sensing data suggests that the $TiO_2$ contents of lunar basalts changed continuously from low-titanium to high-titanium basalts, and medium-titanium basalts (4.5–7.5 wt%, Giguere et al., 2000) are not sampled by any Apollo and Luna mission (Charette et al., 1974; Pieters, 1978).

We compared the FeO and $TiO_2$ contents of each stratigraphic unit in Sinus Iridum with those of all typical kinds of lunar basalts collected by Apollo and Luna missions (Fig. 12). The older Imbrian-aged basalts (Im1 and Im2) have relatively lower $TiO_2$ contents, similar with the Apollo 15 low-titanium basalts collected in the southeastern Mare Imbrium. But basalts in Sinus Iridum are less iron-rich than the Apollo 15 basalts. The younger Eratosthenian-aged basalts (Em2 and Em1) have relatively higher $TiO_2$ contents, but still lower than Apollo 11 and 17 high-titanium basalts. Therefore, these basalts can be classified as medium-titanium basalts (Giguere et al., 2000). Surface in-situ exploration or even future sample-return exploration in the Sinus Iridum region can fill the gap in medium-titanium basalts of Apollo and Luna missions. While the reader should be aware of the current debates on accuracy of the Lucey algorithms (e.g, Wilcox et al., 2005; Bugiolacchi and Guest, 2008), which caution us to be carefully in interpreting results from orbiter spectral data and the importance and urgency to get new "ground truth" of lunar surface from new missions like the Chinese Chang'E-3 (CE-3) mission and future sample-return missions. These future exploration results can be comprehensively compared with results of this study, which is significant for the validation of models and methods related to lunar remote sensing.

### 6.3. Origin of olivine-rich materials within Sinus Iridum

Using $M^3$ imaging spectrometer data, we found some olivine-rich rocks in the northern wall of Sinus Iridum, which was consistent with the results of Yamamoto et al. (2010). These olivine-rich rocks may indicate some deep-source materials and is thus significant for constraining earlier geological evolutionary history of this region. According to the lunar magma ocean hypothesis (e.g., Elkins Tanton et al., 2002), olivine would crystallize very early and accumulate in the lower lunar mantle during the crystallization differentiation process. These olivine could then be transported to the surface in three ways: (1) large impact events would penetrate the lunar crust and excavate olivine from the mantle (Yamamoto et al., 2010; Pieters, 1982), (2) solid olivine might transfer with melted magma as inclusions and erupt to the surface through volcanic activities, (3) these olivine could intrude into shallow crust and then be excavated by small impacting or slumping. The latest inversion result from GRAIL gravity data suggested that the crustal thickness in Mare Imbrium is very thin of about 10 km (Wieczorek et al., 2012). The large impact generating the Mare Imbrium might have penetrated the primordial lunar crust and excavated mantle materials. We suggest the northern Sinus Iridum olivine-rich materials may originate from direct excavation of lunar mantle materials by the large impact that formed the Mare Imbrium.

### 6.4. Geological evolutionary history in Sinus Iridum

Based on the stratigraphic definition and dating results in this study and previous geological mapping results (Schaber, 1969), we created a new geological map for Sinus Iridum (Fig. 13) and sorted out the geological evolutionary history of this region:

1. About 3.85 Ga ago, a large impact generated the multi-ring structural Imbrium Basin (e.g. Ryder, 2002).
2. After about 10 Ma of the Imbrium impact (3.84–3.7 Ga), a discrete impact formed the primitive Iridum Crater (Wagner et al., 2002). Massive impact ejecta accumulated around the crater, and formed the crater wall (unit Iiw in Fig. 13) and rim crests. The rim crests can be classified into two groups: the hummocky rim materials near the crater (unit Iirh in Fig. 13) and radial rim materials far from the crater (unit Iirr in Fig. 13), most parts of the rim crests composed the present Montes Jura.
3. During near 1.2 Ga after the Sinus Iridum impact, the Sinus Iridum region had experienced four episodes of major magmatic activity. The model ages of the four magmatic activities are determined as 3.32 Ga, 3.20～3.21 Ga, 3.09 Ga and 2.50 Ga respectively. The basalts filled by magmatic activities covered the primitive crater floor and outer ring of the Imbrium basin. The four episodes of magmatic activity generally evolved from low-titanium and low-olivine to medium-titanium and high-

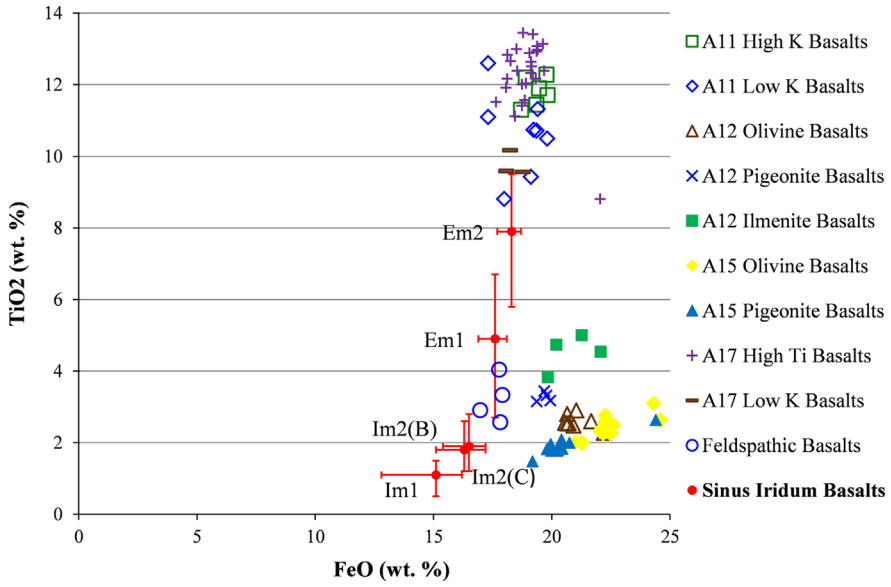



**Fig. 12.** Comparation of iron and titanium content for basalts in the Sinus Iridum and northwest Mare Imbrium with all typical kinds of lunar basalts. For Sinus Iridum and northwest Mare Imbrium, the center value represents the mean value of each basaltic unit and error bars describe the threshold value for defining homogeneous units.

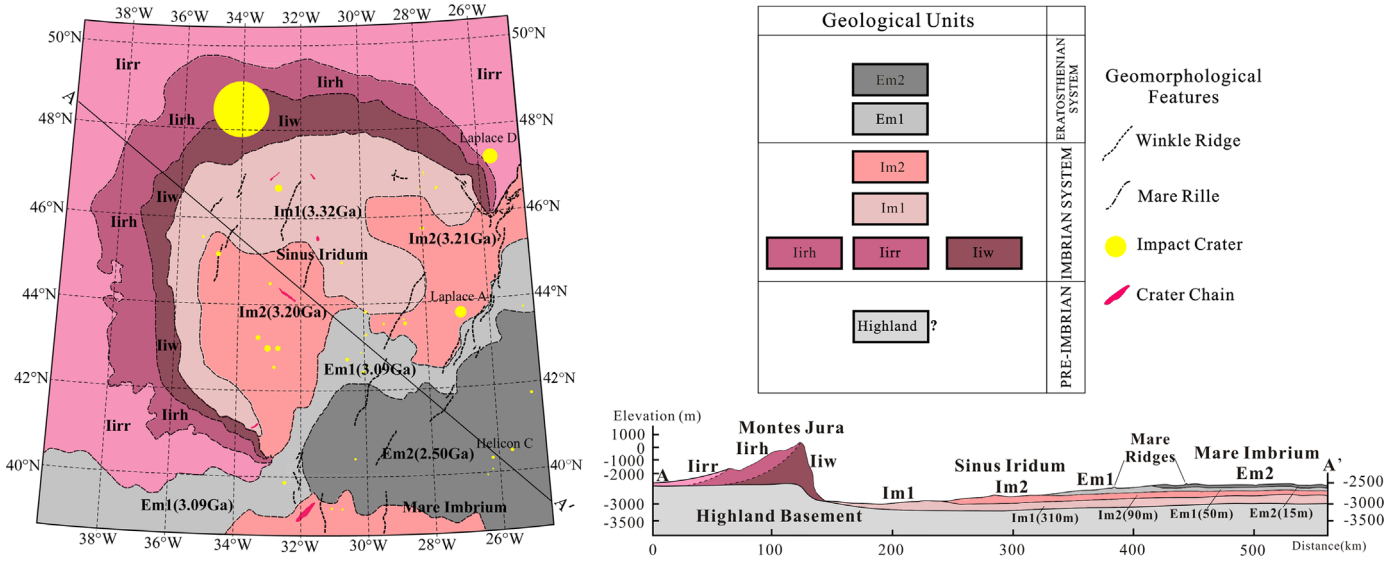



**Fig. 13.** Geological map of Sinus Iridum. This map mainly displays the stratigraphic definition and dating results, and extract one stratigraphic profile from the northwest to southeast. Numerous small craters in the highland are not displayed. The dashed lines between Iirr, Iirh and Iiw unit in profile A–A' do not represent overlap relationship of these strata, but the accumulated ejecta, The highlands basement are probably pre-Imbrian bedrock (M'Gonigle et al., 1972).

olivine. Additionally, the volume of basalts erupted in the four magmatic activities decreased with time, and the thicknesses of these mare basalts are about 106 m, 49 m, 38 m and 17 m respectively. During the magmatic activities, the lava flows eroded the lunar surface and formed the lunar sinuous rilles.

4. Around about 2.5 Ga, the magmatic activity ceased and later tectonic activities generated some wrinkle ridges on the surface. Then, meteorite impact became the major geological processes that modified the landscapes of lunar surface, and generated a great mount of small craters.

### 6.5. *Candidate landing sites for the future Chinese missions*

On the basis of topography analyses results and the experiences of landing sites selection of previous lunar and martian landing exploration missions (Arvidson et al., 2008; Bridges, 2003; Golombek et al., 1997; Grant et al., 2011; Kirk et al., 2008; Quaide and Oberbeck, 1969; Wilhelms, 1985), we proposed two specific candidate landing sites for the future Chinese missions. These landing sites should have relatively low topographic slope ( $< 1.0^{\circ}$), small surface roughness ( $\leq 1.0$ m, LOLA RMS height), low rock abundance ( $< 0.5\%$, data from Bandfield et al., 2011), and low crater density (few large craters exist). To maximize the possible scientific results from the missions, these proposed landing sites should be near to abundant geomorphological features and/or unique material type. One of our proposed landing sites is located in the northeastern corner of Sinus Iridum, where the longest rille in Sinus Iridum region is cross-cut by the longest wrinkle ridge. The other suggestion would be in the central Sinus Iridum region, where three mare basalt units with different ages intersect. The basic topographic and geological parameter of these two recommended landing sites and the six Apollo mission landing sites are listed in Table 4.

**Table 4**
Topographic and geological parameters of two proposed landing sites for the Chinese future missions and the six Apollo missions' landing sites.

| Location | Site 1 Sinus Iridum | Site 2 Sinus Iridum | Apollo 11 Mare Tranquillitatis | Apollo12 Oceanus Procellarum | Apollo14 Fra Mauro | Apollo15 Hadley-Apennines | Apollo16 Descartes | Apollo17 Taurus-Littrow |
|---|---|---|---|---|---|---|---|---|
| Lat., Long. | 45.89°N 25.91°W | 44.01°N 30.35°W | 0.93°N, 23.43°E | 3.20°S 23.39°W | 3.67°S 17.47°W | 26.10°N 3.65°E | 8.99°S 15.51°E | 20.17°N 30.77°E |
| Elevation (LOLA) | −2577 | −2714 | −1972 | −1459 | −1052 | −1937 | 1 | 2642 |
| Terrain slope [a] | 0.8 | 0.1 | 0.1 | 0.2 | 0.3 | 0.6 | 0.3 | 2.0 |
| Roughness [b] | 0.8 | 0.8 | 1.0 | 0.8 | 0.9 | 1.0 | 1.3 | 1.4 |
| Rock abundance [c] | 0.003 | 0.001 | 0.004 | 0.006 | 0.003 | 0.003 | 0.003 | 0.012 |
| FeO content [d] | 16.5 | 15.8 [e] | 18.0 | 16.7 | 13.2 | 14.8 | 5.3 | 16.6 |
| $TiO_2$ content [d] | 2.0 | 1.7 [e] | 11.0 | 5.8 | 2.2 | 2.1 | 1.0 | 6.9 |

[a] Terrain slope calculated from 1024 pixel/degree LOLA topography data (Section 3.1).
[b] Roughness value from Smith at al. (2010), as describe in Section 3.1.
[c] Rock abundance value from Bandfield et al., (2011).
[d] FeO and $TiO_2$ content calculated from Clementine UVVIS data using Lucey et al.'s method (Section 3.2).
[e] The Clementine UVVIS data does not cover Sits 2, FeO and $TiO_2$ contents are average value of surrounding pixels.

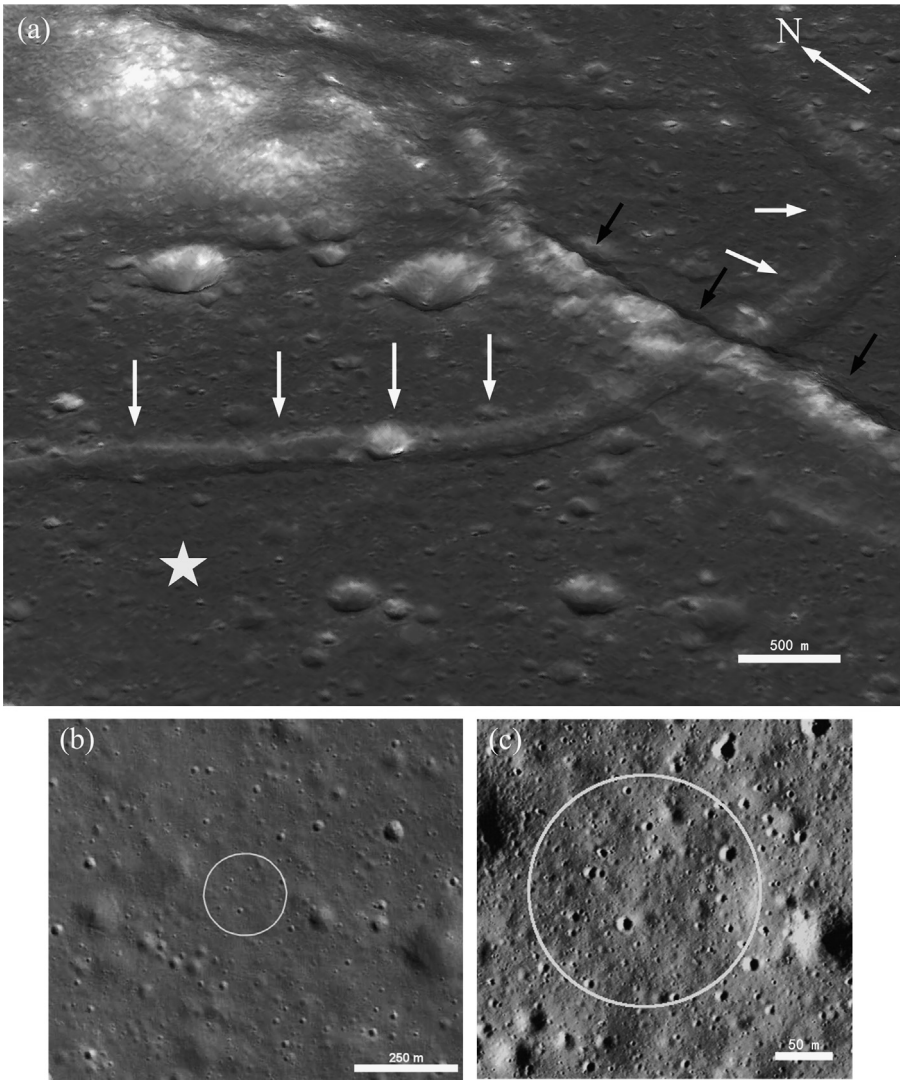



**Fig. 14.** Proposed landing site (centered at 45.89°N, 25.93°W) in the northeast corner of Sinus Iridum. (a) 3-D view map of the first proposed landing site and surrounding region, with SELENE TC orthoimage (TCO_MAP_02_N48E333N45E336SC) overlying TC Digital Terrain Model data (DTM_MAP_02_N48E333N45E336SC). The white arrows point to sinuous rille and the black arrows point to wrinkle ridge. The light-color uplift block at the north is the Promontorium Laplace. The map scale is only true along its direction and the vertical exaggeration factor is 2.5. (b) Local detailed image of the first proposed landing site and surrounding area (LROC NAC frame M104690472RE, spatial resolution: ~1.7 m/pixel). (c) High resolution image of the landing target (LROC NAC frame M177798556LE, spatial resolution: ~1 m/pixel ). The white star in a, and white circle in b and c represent the proposed landing target site for Chang'E-3 mission, with a diameter of about 200 m, and up is the north for (b) and (c). All the map projection is Lambert conformal projection and centered at the proposed landing site.

*6.5.1. Northeast ridge-rille site*

The first proposed landing target site (Site 1) locates in the northeastern corner inside Sinus Iridum (centered at 45.89°N, 25.91°W). Although various kinds of geomorphological features are present near this site, the small-scale (200 m circle) topographic feature appears safe for landing exploration missions. The topographic slope and roughness are less than the threshold values for landing site selection (Table 4). On the high resolution LROC NAC image (~1 m/pixel) of Site 1 (Fig. 14 c), only four craters with diameter of ~10 m are present in the 200 m circle proposed landing site. A relatively benign landing site is also demonstrated by the derived rock abundance value for these regions of Bandfield et al. (2011), which is not greater than all six Apollo landing sites.

Moreover, this proposed landing site also has great science potential. The longest sinuous rille (about 1.2 km north of Site 1, Section 4.4.2) and wrinkle ridge (about 2.8 km northeast of Site 1, Section 4.4.1) within Sinus Iridum are present near the proposed landing site (Fig. 14a). The lunar rover can thus investigate these landforms in unprecedented details with in-situ cameras, like Panoramic Camera aboard CE-3 lunar rover (Yang, 2009). The superposition and cross-cutting relations of the rille and ridge suggest the complex tectonic activities in this region, including magmatic and tectonic activities. Subsurface exploring instruments, like ground penetrating radar (GPR) onboard CE-3's rover (Fa, 2013), could build up the 3-D profiles of the subsurface, which may have significant potential for advancing our knowledge of

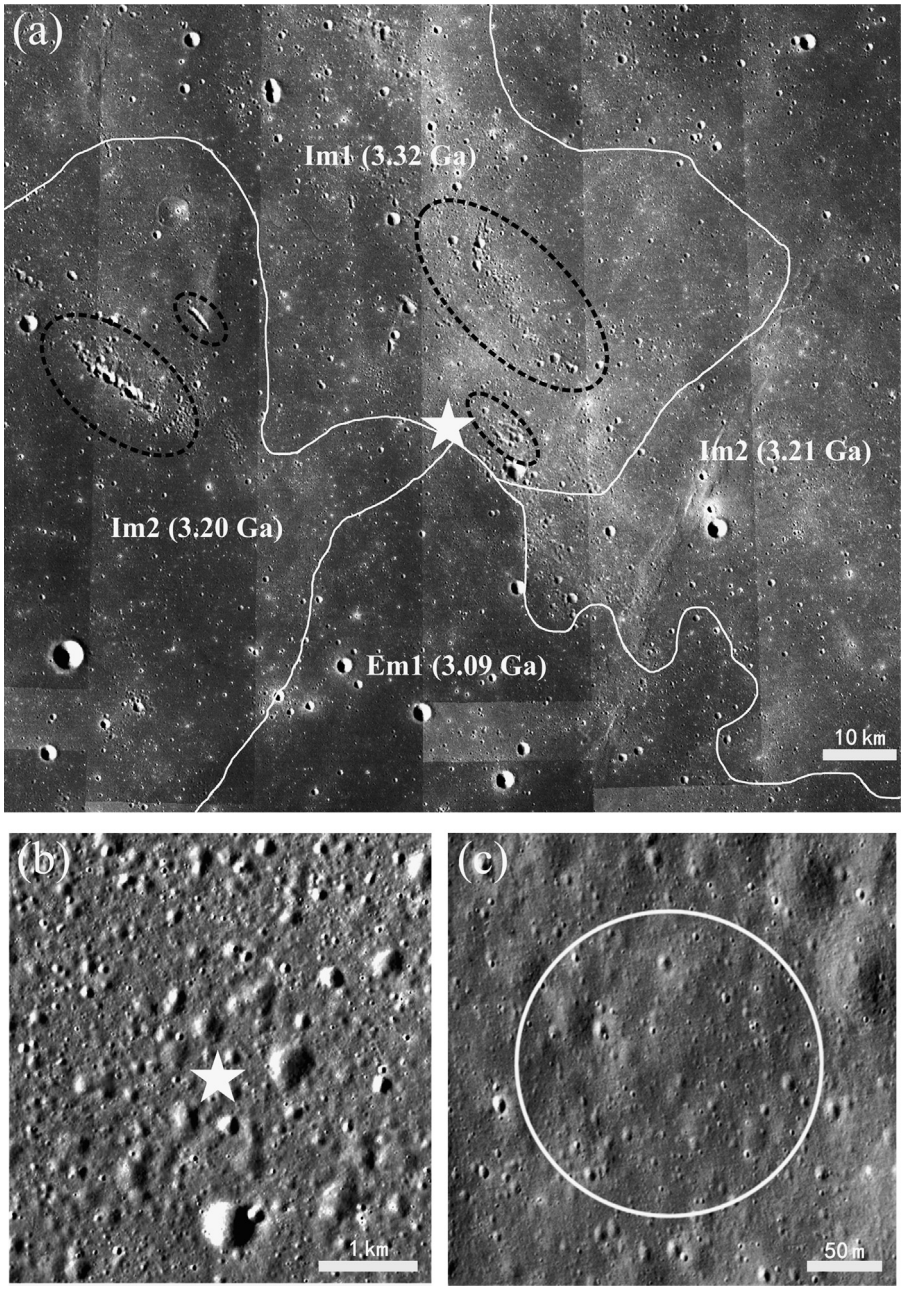



**Fig. 15.** Proposed landing site (centered at 44.01°N, −30.35°W) in the central Sinus Iridum region. (a) LROC WAC mosaic map of the landing site and surrounding areas (centered at 43.98°N, −30.12°W). (b) SELENE TC morning map of the landing site (TC TCO_MAPm04_N45E327N42E330SC). (c) High resolution of the inner landing site (LROC NAC frame M160153704RE, spatial resolution: ~0.64 m/pixel). The white curves in (a) represent the boundaries of geological units defined in Section 5, and the letters label the units' name and surface model ages dated in this study (Section 5). The black dashed ellipses mark craters chains. The white star in a and b, and white circles in c represent the proposed landing site. All the map projection is Lambert conformal projection and centered at the proposed landing site, and up is the north.

origin and mechanism of lunar wrinkle ridges and tectonic activities.

#### 6.5.2. Central landing site

The second proposed landing site (Site 2) is in the central Sinus Iridum (centered at 44.01°N, 30.35°W). This site appears much safer for landing exploration than Site 1 and the six Apollo landing sites according to basic topographic parameters (Table 4). Although this site is surrounded by several relatively large craters with maximum diameter of about 600 m at a distance of ~2 km (Fig. 15 b, SELENE TC image, 10 m/pixel), the inside site area is very smooth, only four small craters with diameters of ~6 to 10 m are visible within the proposed 200 m circle landing site (Fig. 15c).

This proposed site is also scientifically significant with unique geological features. This site is close to the boundaries of three mare basalt units, i.e., Im1, Im2 and Em1 defined in Section 5.1, corresponding to the earlier three magmatic activities (Fig. 15a). The nearest basalt unit boundary is only 2 km away form Site 2. In-situ compositional analyses of these basalts with instruments onboard future lunar rovers, like Alpha Particle X-Ray Spectrometer (APXS) and Visible and Near-infrared Imaging Spectrometer (VNIS) onboard the CE-3's rover (Liang et al., 2013; Liu et al., 2013; Ma and Wang, 2011), may reveal compositional characteristics of regional magmatic evolution and lunar late-stage volcanism. This site is also near to some linear and clustered secondary crater chains (Fig. 15a) probably formed by ejecta from large carters of Copernican ages, e.g., Copernicus, Aristillus and Aristarchus (Schaber, 1969). These large craters may have excavated the primordial crust materials. The lunar highland rock fragments found in the Apollo 11 bulk regolith sample directly led to the lunar magma ocean hypothesis, which is now the most commonly accepted hypothesis for lunar crustal formation (e.g., Wood et al., 1970). Future Chinese missions may detect some primordial crust materials, of which in-situ compositional analyses may get some important constraints on the chemical characteristics of primordial lunar magma ocean.

## 7. Concluding remarks

We systematically studied the topographic, compositional, stratigraphic, and geological features within the Sinus Iridum using newly obtained remote sensing data. The major finding of this paper are summarized as the followings:

(1) The Sinus Iridum and northwestern Mare Imbrium have similar elevations, but the surface elevation within Sinus Iridum decreases for about 500 m from southeast to northwest. Over eighty percent of areas within Sinus Iridum have a slope of lower than one degree. The surface roughness for over ninety percent of the inner Sinus Iridum region is lower than 1.3 m, there are generally few discrete positive relief features, such as large-scale outcrops or large boulders ( > 2 m diameter), in the region. The flat and smooth topography of Sinus Iridum can provide excellent safety for the future Chinese robotic and human missions.

(2) The Sinus Iridum and northwestern Mare Imbrium region have experienced four episodes of major magmatic activity with model ages from 3.20 Ga to 2.50 Ga. The older Imbrian-aged basalts in the northern Sinus Iridum (Im1 and Im2) are mainly low-titanium basalts, and the younger Eratosthenian-aged basalts in the southern Sinus Iridum and northwestern Mare Imbrium (Em2 and Em1) are medium-titanium basalts with a relatively high abundant of olivine. The volume of basalts erupted in the four magmatic activities decreased with time, with thickness of basaltic strata varying from 106 m to 17 m.

(3) The materials within Sinus Iridum are mainly composed of mature and pyroxene-rich basalts. Some fresh pyroxene-rich basalts excavated from the near-surface are visible at the wall of some fresh craters. The surrounding highland areas have a feldspar-dominated composition. Some possible olivine-rich rocks directed excavated from lunar mantle are detected at the northern wall of Sinus Iridum.

(4) The Sinus Iridum region has various kinds of landforms and a complex geologic evolutionary history. Integrating the requirement of safe landing and the largest outcome of potential science findings, we have proposed two potential landing sites for the future Chinese robotic and human missions.

## Acknowledgments

The authors are grateful to the Editor Dr. Sridevi Ganesh and the anonymous reviewer for thoughtful and constructive comments in their review of this paper. The authors also would like to thank Dr. Zhiyong Xiao for helpful revise. This study was supported by the National Natural Science Foundation of China (41072045) and the National Basic Research Program of China (2010CB808906).

## References

Adams, J.B., 1974. Visible and near-infrared diffuse reflectance spectra of pyroxenes as applied to remote sensing of solid objects in the solar system. J. Geophys. Res. 79, 4829–4836.

Adams, J.B., Goullaud, L.H., 1978. Plagioclase feldspars-visible and near infrared diffuse reflectance spectra as applied to remote sensing, In: Proceedings of the Lunar and Planetary Science Conference, pp. 2901–2909.

Arvidson, R., Adams, D., Bonfiglio, G., Christensen, P., Cull, S., Golombek, M., Guinn, J., Guinness, E., Heet, T., Kirk, R., Knudson, A., Malin, M., Mellon, M., McEwen, A., Mushkin, A., Parker, T., Seelos, F., Seelos, K., Smith, P., Spencer, D., Stein, T., Tamppari, L., 2008. Mars Exploration Program 2007 Phoenix landing site selection and characteristics. J. Geophys. Res., 113.

Arvidson, R., Boyce, J., Chapman, C., Cintala, M., Fulchignoni, M., Moore, H., Neukum, G., Schultz, P., Soderblom, L., Strom, R., 1979. Standard techniques for presentation and analysis of crater size-frequency data. Icarus 37, 467–474.

Bandfield, J.L., Ghent, R.R., Vasavada, A.R., Paige, D.A., Lawrence, S.J., Robinson, M.S., 2011. Lunar surface rock abundance and regolith fines temperatures derived from LRO Diviner Radiometer data. J. Geophys. Res.: Planets 1991–2012, 116.

Bridges, J.C., 2003. Selection of the landing site in Isidis Planitia of Mars probe Beagle 2. J. Geophys. Res., 108.

Boardman, J.W., Pieters, C.M., Green, R.O., Lundeen, S.R., Varanasi, P., Nettles, J., Petro, N., Isaacson, P., Besse, S., Taylor, L.A., 2011. Measuring moonlight: an overview of the spatial properties, lunar coverage, selenolocation, and related Level 1B products of the Moon Mineralogy Mapper. J. Geophys. Res.-Planet, 116.

Bugiolacchi, R., Guest, J.E., 2008. Compositional and temporal investigation of exposed lunar basalts in the Mare Imbrium region. Icarus 197, 1–18.

Carr, M.H., 1974. The role of lava erosion in the formation of lunar rilles and Martian channels. Icarus 22, 1–23.

Charette, M.P., McCord, T.B., Pieters, C., Adams, J.B., 1974. Application of remote spectral reflectance measurements to lunar geology classification and determination of titanium content of lunar soils. J. Geophys. Res. 79, 1605–1613.

Cheek, L.C., Pieters, C.M., Boardman, J.W., Clark, R.N., Combe, J.P., Head, J.W., Isaacson, P.J., McCord, T.B., Moriarty, D., Nettles, J.W., Petro, N.E., Sunshine, J.M., Taylor, L.A., 2011. Goldschmidt crater and the Moon's north polar region: results from the Moon Mineralogy Mapper ($M^3$). J. Geophys. Res. 116, E00G02.

Chen, S.B., Meng, Z.G., Cui, T.F., Lian, Y., Wang, J.R., Zhang, X.Q., 2010. Geologic investigation and mapping of the Sinus Iridum quadrangle from Clementine, SELENE, and Chang'e-1 data. Sci. China Phys., Mech. Astron. 53, 2179–2187.

Elkins Tanton, L.T., Van Orman, J.A., Hager, B.H., Grove, T.L., 2002. Re-examination of the lunar magma ocean cumulate overturn hypothesis: melting or mixing is required. Earth Planet. Sci. Lett. 196, 239–249.

Fa, W., 2013. Simulation for ground penetrating radar (GPR) study of the subsurface structure of the Moon. J. Appl. Geophys. 99, 98–108.

Giguere, T.A., Taylor, G.J., Hawke, B., Lucey, P.G., 2000. The titanium contents of lunar mare basalts. Meteorit. Planet. Sci. 35, 193–200.

Gillis, J.J., Jolliff, B.L., Elphic, R.C., 2003. A revised algorithm for calculating $TiO_2$ from Clementine UVVIS data: a synthesis of rock, soil, and remotely sensed $TiO_2$ concentrations. J. Geophys. Res. 108, 01515.

Golombek, M., Plescia, J., Franklin, B., 1991. Faulting and folding in the formation of planetary wrinkle ridges, In: Proceedings of the Lunar and Planetary Science Conference, pp. 679–693.
Golombek, M.P., Cook, R.A., Moore, H.J., Parker, T.J., 1997. Selection of the Mars Pathfinder landing site. J. Geophys. Res. 102, 3967.
Gong, X., Jin, Y.Q., 2012. Diurnal physical temperature at Sinus Iridum area retrieved from observations of Chinese Chang'E-1 microwave radiometer. Icarus 218, 807–816.
Grant, J.A., Golombek, M.P., Grotzinger, J.P., Wilson, S.A., Watkins, M.M., Vasavada, A.R., Griffes, J.L., Parker, T.J., 2011. The science process for selecting the landing site for the 2011 Mars Science Laboratory. Planet. Space Sci. 59, 1114–1127.
Haruyama, J., Hara, S., Hioki, K., Iwasaki, A., Morota, T., Ohtake, M., Matsunaga, T., Araki, H., Matsumoto, K., Ishihara, Y., 2012. Lunar global digital terrain model dataset produced from SELENE (Kaguya) terrain camera stereo observations, In: Proceedings of the Lunar and Planetary Institute Science Conference Abstracts, p. 1200.
Haruyama, J., Matsunaga, T., Ohtake, M., Morota, T., Honda, C., Yokota, Y., Torii, M., Ogawa, Y., Grp, L.W., 2008. Global lunar-surface mapping experiment using the Lunar Imager/Spectrometer on SELENE. Earth Planets Space 60, 243–255.
Hiesinger, H., Jaumann, R., Neukum, G., Head III, J.W., 1998. On the relation of age and titanium content of lunar mare basalts. In: Proceedings of the Lunar and Planetary Science Conference Abstract #1243.
Hiesinger, H., Jaumann, R., Neukum, G., Head III, J.W., 2000. Ages of mare basalts on the lunar nearside. J. Geophys. Res. 105, 29239–29275.
Huang, J., Xiao, L., Yang, J., Dong, Y., 2010. New Model Ages of Mare Material in Sinus Iridum, Moon, Lunar and Planetary Institute Science Conference Abstracts, p. 1184.
Hulme, G., 1973. Turbulent lava flow and the formation of lunar sinuous rilles. Mod. Geol. 4, 107–117.
Hulme, G., 1982. A review of lava flow processes related to the formation of lunar sinuous rilles. Geophys. Surv. 5, 245–279.
Hurwitz, D.M., Head, J.W., Wilson, L., Hiesinger, H., 2012. Origin of lunar sinuous rilles: modeling effects of gravity, surface slope, and lava composition on erosion rates during the formation of Rima Prinz. J. Geophys. Res. 117, E00H14.
Hurwitz, D.M., Head, J.W., Hiesinger, H., 2013. Lunar sinuous rilles: distribution, characteristics, and implications for their origin. Planet. Space Sci. 79–80, 1–38.
Kaula, W.M., Head, J.W., Merrill, R.B., Pepin, R.O., Solomon, S.C., Walker, D., Wood, C.A., 1981. Basaltic Volcanism on the Terrestrial Planets. Pergamon Press, New York.
Kirchoff, M.R., Chapman, C.R., Marchi, S., Curtis, K.M., Enke, B., Bottke, W.F., 2013. Ages of large lunar impact craters and implications for bombardment during the Moon's middle age. Icarus 225, 325–341.
Kirk, R., Howington-Kraus, E., Rosiek, M., Anderson, J., Archinal, B., Becker, K., Cook, D., Galuszka, D., Geissler, P., Hare, T., 2008. Ultrahigh resolution topographic mapping of Mars with MRO HiRISE stereo images: meter-scale slopes of candidate Phoenix landing sites. J. Geophys. Res. 113, E00A24.
Liang, X.H., Wu, M.Y., Wang, H.Y., Peng, W.X., Zhang, C.M., Cui, X.Z., Wang, J.Z., Zhang, J.Y., Yang, J.W., Fan, R.R., Gao, M., Liu, Y.Q., Zhang, F., Dong, Y.F., Guo, D.Y., 2013. Near infrared distance sensing method for Chang E-3 Alpha Particle X-Ray Spectrometer. Spectrosc. Spectr. Anal. 33, 1360–1363 (Chinese article with English abstract).
Liu, B., Liu, J.-Z., Zhang, G.-L., Ling, Z.-C., Zhang, J., He, Z.-P., Yang, B.-Y., Zou, Y.-L., 2013. Reflectance conversion methods for the VIS/NIR imaging spectrometer aboard the Chang'E-3 lunar rover: based on ground validation experiment data. Res. Astron. Astrophys. 13, 862–874.
Lucey, P.G., Blewett, D.T., Hawke, B.R., 1998. Mapping the FeO and $TiO_2$ content of the lunar surface with multispectral imagery. J. Geophys. Res. 103, 3679–3699.
Lucey, P.G., Blewett, D.T., Jolliff, B.L., 2000. Lunar iron and titanium abundance algorithms based on final processing of Clementine ultraviolet–visible images. J. Geophys. Res. 105, 20297–20305.
Lucey, P.G., Taylor, G.J., Malaret, E., 1995. Abundance and distribution of iron on the Moon. Science 268, 1150–1153.
M'Gonigle, J.W., Schleicher, D., Chart, A., 1972. Geologic map of the Plato quadrangle of the Moon, 1-701 (LAC-I2), US Geological Survey.
Ma, R.M., Wang, H.Y., 2011. Research on data compression of the X-Ray Spectrometer for Chang'E mission. J. Astron. 32, 104–108 (Chinese article with English abstract).
Maune, D.F., 2007. Digital elevation model technologies and applications: the DEM users manual, 2nd ed. Asprs Publications, Bethesda.
Maxwell, T.A., 1978, Origin of multi-ring basin ridge systems-an upper limit to elastic deformation based on a finite-element model, In: Proceedings of the Lunar and Planetary Science Conference, vol. 9, p. 3541–3559.
McEwen, A., Robinson, M., 1997. Mapping of the Moon by Clementine. Adv. Space Res. 19, 1523–1533.
Melosh, H.J., 1989. Impact Cratering: A Geologic Process. Oxford University Press, New York p. 78.
Michael, G., Neukum, G., 2010. Planetary surface dating from crater size–frequency distribution measurements: Partial resurfacing events and statistical age uncertainty. Earth Planet. Sci. Lett. 294, 223–229.
Morota, T., Haruyama, J., Ohtake, M., Matsunaga, T., Honda, C., Yokota, Y., Kimura, J., Ogawa, Y., Hirata, N., Demura, H., Iwasaki, A., Sugihara, T., Saiki, K., Nakamura, R., Kobayashi, S., Ishihara, Y., Takeda, H., Hiesinger, H., 2011. Timing and characteristics of the latest mare eruption on the Moon. Earth Planet. Sci. Lett. 302, 255–266.
Mustard, J.F., Pieters, C.M., Isaacson, P.J., Head, J.W., Besse, S., Clark, R.N., Klima, R.L., Petro, S., Staid, M.I., Sunshine, J.M., Runyon, C.J., Tompkins, S., 2011. Compositional diversity and geologic insights of the Aristarchus crater from Moon Mineralogy Mapper data. J. Geophys. Res. 116, E00G12.
Neukum, G., Ivanov, B.A., Hartmann, W.K., 2001. Cratering records in the inner solar system in relation to the lunar reference system. Space Sci. Rev. 96, 55–86.
Neumann, G., Abshire, J., Aharonson, O., Garvin, J., Sun, X., Zuber, M., 2003. Mars Orbiter Laser Altimeter pulse width measurements and footprint-scale roughness. Geophys. Res. Lett. 30, 1561.
Nozette, S., Rustan, P., Pleasance, L., Kordas, J., Lewis, I., Park, H., Priest, R., Horan, D., Regeon, P., Lichtenberg, C., 1994. The Clementine mission to the Moon: scientific overview. Science 266, 1835.
Papike, J.J., Hodges, F.N., Bence, A.E., Cameron, M., Rhodes, J.M., 1976. Mare basalts: Crystal chemistry, mineralogy, and petrology. Rev. Geophys. 14, 475–540.
Pieters, C.M., 1978. Mare Basalt types on the front side of the moon: a summary of spectral reflectance data, In: Proceedings of the 9th Lunar and Planetary Science Conference, New York, Pergamon Press, Inc., Houston, Texas, pp. 2825–2849.
Pieters, C.M., 1982. Copernicus crater central peak- Lunar mountain of unique composition. Science 215, 59–61.
Pieters, C., Fischer, E., Rode, O., Basu, A., 1993. Optical effects of space weathering: the role of the finest fraction. J. Geophys. Res.: Planets 1991–2012 (98), 20817–20824.
Pieters, C.M., Boardman, J., Buratti, B., Chatterjee, A., Clark, R., Glavich, T., Green III, R.J.H., Isaacson, P., Malaret, E., McCord, T., Mustard, J., Petro, N., Runyon, C., Staid, M., Sunshine, J., Taylor, L., Tompkins, S., Varanasi, P., White, M., 2009. The Moon Mineralogy Mapper ($M^3$) on Chandrayaan-1. Curr. Sci., 96.
Qiu, J., Stone, R., 2013. Chinese Mission Ushers in new era of lunar exploration. Science 342, 1026.
Quaide, W., Oberbeck, V., 1969. Geology of the Apollo landing sites. Earth-Sci. Rev. 5, 255–278.
Robinson, M., Brylow, S., Tschimmel, M., Humm, D., Lawrence, S., Thomas, P., Denevi, B., Bowman-Cisneros, E., Zerr, J., Ravine, M., 2010. Lunar reconnaissance orbiter camera (LROC) instrument overview. Space Sci. Rev. 150, 81–124.
Rosenburg, M.A., Aharonson, O., Head, J.W., Kreslavsky, M.A., Mazarico, E., Neumann, G.A., Smith, D.E., Torrence, M.H., Zuber, M.T., 2011. Global surface slopes and roughness of the Moon from the lunar orbiter laser altimeter. J. Geophys. Res. 116, E02001.
Ryder, G., 2002. Mass flux in the ancient Earth–Moon system and benign implications for the origin of life on Earth. J. Geophys. Res. 107, 5022.
Scholten, F., Oberst, J., Robinson M.S., 2011. GLD100 – Lunar topography from LROC WAC stereo, EPSC-DPS Joint Meeting, Nantes, France.
Scholten, F., Oberst, J., Matz, K.D., Roatsch, T., Wählisch, M., Speyerer, E., Robinson, M., 2012. GLD100: The near-global lunar 100 m raster DTM from LROC WAC stereo image data. J. Geophys. Res. 117, E00H17.
Schaber, G., 1969. Geologic map of the Sinus Iridum quadrangle of the Moon, 1-602 (LAC-24):. US Geological Survey, Washington, D.C.
Shepard, M.K., Campbell, B.A., Bulmer, M.H., Farr, T.G., Gaddis, L.R., Plaut, J.J., 2001. The roughness of natural terrain: A planetary and remote sensing perspective. J. Geophys. Res. 106, 32777–32795.
Siewert, J., Ferlito, C., 2008. Mechanical erosion by flowing lava. Contemp. Phys. 49, 43–54.
Smith, D., Zuber, M., Jackson, G., Cavanaugh, J., Neumann, G., Riris, H., Sun, X., Zellar, R., Coltharp, C., Connelly, J., Katz, R., Kleyner, I., Liiva, P., Matuszeski, A., Mazarico, E., McGarry, J., Novo-Gradac, A.-M., Ott, M., Peters, C., Ramos-Izquierdo, L., Ramsey, L., Rowlands, D., Schmidt, S., Scott, V., Shaw, G., Smith, J., Swinski, J.-P., Torrence, M., Unger, G., Yu, A., Zagwodzki, T., 2010a. The Lunar Orbiter Laser Altimeter investigation on the Lunar Reconnaissance Orbiter mission. Space Sci. Rev. 150, 209–241.
Smith, D.E., Zuber, M.T., Neumann, G.A., Lemoine, F.G., Mazarico, E., Torrence, M.H., McGarry, J.F., Rowlands, D.D., Head III, J.W., Duxbury, T.H., 2010b. Initial observations from the Lunar Orbiter Laser Altimeter (LOLA). Geophys. Res. Lett. 37, L18204.
Snyder, J.P., 1987. Map Projections—A Working Manual. US Government Printing Office, Washington p. 42.
Spudis, P.D., Swann, G.A., Greeley, R., 1988. The formation of Hadley Rille and implications for the geology of the Apollo 15 region, In: Proceedings of the Lunar and Planetary Science Conference, pp. 243–254.
Staid, M.I., Pieters, C.M., Besse, S., Boardman, J., Dhingra, D., Green, R., Head, J.W., Isaacson, P., Klima, R., Kramer, G., Mustard, J.M., Runyon, C., Sunshine, J., Taylor, L.A., 2011. The mineralogy of late stage lunar volcanism as observed by the Moon Mineralogy Mapper on Chandrayaan-1. J. Geophys. Res. 116, E00G10.
Strom, R.G., 1972. Lunar mare ridges, rings and volcanic ring complexes, The moon. Springer, pp. 187–215.
Taylor, J., Warren, P., Ryder, G., Delano, J., Pieters, C., Lofgren, G., 1991. Lunar rocks. In: Heiken, G., Vaniman, D., French, B. (Eds.), Lunar Source Book. Cambridge University Press, Cambridge, pp. 183–284.
Thomson, B.J., Grosfils, E.B., Bussey, D.B.J., Spudis, P.D., 2009. A new technique for estimating the thickness of mare basalts in Imbrium Basin. Geophys. Res. Lett. 36, L12201.
van Gasselt, S., Nass, A., 2014. On the concept and integration of geologic time in planetary mapping. In: Buchroithner, M., Prechtel, N., Burghardt, D. (Eds.), Cartography from Pole to Pole. Springer, Berlin Heidelberg, pp. 271–281.
Wagner, R., Head Iii, J., Wolf, U., Neukum, G., 2002. Stratigraphic sequence and ages of volcanic units in the Gruithuisen region of the Moon. J. Geophys. Res. 107, 5104.
Watters, T.R., 2004. Elastic dislocation modeling of wrinkle ridges on Mars. Icarus v. 171, 284–294.

Wieczorek, M.A., Neumann, G.A., Nimmo, F., Kiefer, W.S., Taylor, G.J., Melosh, H.J., Phillips, R.J., Solomon, S.C., Andrews-Hanna, J.C., Asmar, S.W., 2012. The crust of the Moon as seen by GRAIL. Science 339, 671–675.
Wilcox, B., Lucey, P., Gillis, J., 2005. Mapping iron in the lunar mare: An improved approach. J. Geophys. Res.: Planets 1991–2012, 110.
Wilhelms, D., 1985. Selection of the Apollo 15 landing site. Geol. Apollo 15 Land. Site, 73–75.
Williams, D.A., Fagents, S.A., Greeley, R., 2000. A reassessment of the emplacement and erosional potential of turbulent, low-viscosity lavas on the Moon. J. Geophys. Res.: Planets 1991–2012 (105), 20189–20205.
Wilson, L., Head, J.W., 1981. Ascent and eruption of basaltic magma on the Earth and Moon. J. Geophys. Res.: Solid Earth 1978–2012 (86), 2971–3001.
Wood, J.A., Dickey Jr, J., Marvin, U.B., Powell, B., 1970. Lunar anorthosites and a geophysical model of the Moon. In: Proceedings of the Apollo 11 Lunar Science Conference, p. 965–988.
Wu, Y., Xue, B., Zhao, B., Lucey, P., Chen, J., Xu, X., Li, C., Ouyang, Z., 2012. Global estimates of lunar iron and titanium contents from the Chang' E-1 IIM data. J. Geophys. Res. 117, E02001.
Xiao, Z., Strom, R.G., 2012. Problems determining relative and absolute ages using the small crater population. Icarus 220, 254–267.
Xiao, Z., Zeng, Z., Ding, N., Molaro, J., 2013. Mass wasting features on the Moon – how active is the lunar surface? Earth Planet. Sci. Lett. 376, 1–11.
Yamamoto, S., Nakamura, R., Matsunaga, T., Ogawa, Y., Ishihara, Y., Morota, T., Hirata, N., Ohtake, M., Hiroi, T., Yokota, Y., Haruyama, J., 2010. Possible mantle origin of olivine around lunar impact basins detected by SELENE. Nature Geoscience 3, 533–536.
Yang, J., 2009. Chang'E-3 satellite and its optical payloads, In: Proceedings of the 2009 Photonics West Conference (in Chinese).
Zhao, J.N., Huang, J., Xiao, L., Qiao, L., Wang, J., Hu, S.Y., 2013. Crater size-frequency distribution measuremenst and age determination of Sinus Iridum. Earth Sci. 38, 1–11 (in Chinese).
Zou, X., 2011. Topographic analysis of the proposed landing area of Sinus Iridum. Chin. Sci. Bull. 56, 2082–2087.